IMPROVEMENT OF SINGLE-ATOM LOADING EFFICIENCY USING RYDBERG STATE

RATTAKORN KAEWUAM

MASTER OF SCIENCE
IN PHYSICS

GRADUATE SCHOOL
CHIANG MAI UNIVERSITY
JULY 2015

IMPROVEMENT OF SINGLE-ATOM LOADING EFFICIENCY USING RYDBERG STATE

RATTAKORN KAEWUAM

A THESIS SUBMITTED TO CHIANG MAI UNIVERSITY IN PARTIAL FULFILLMENT OF THE REQUIREMENTS FOR THE DEGREE OF MASTER OF SCIENCE IN PHYSICS

GRADUATE SCHOOL, CHIANG MAI UNIVERSITY

JULY 2015

IMPROVEMENT OF SINGLE-ATOM LOADING EFFICIENCY USING RYDBERG STATE

RATTAKORN KAEWUAM

THIS THESIS HAS BEEN APPROVED TO BE A PARTIAL FULFILLMENT OF
THE REQUIREMENTS FOR THE DEGREE OF
MASTER OF SCIENCE
IN PHYSICS

Examination Committee:

.....Chairman
(Asst. Prof. Dr. Sarayut Deachapunya)

.....Member
(Dr. Waranont Anukool)

.....Member
(Dr. Narupon Chattrapiban)

Advisor:

.....
(Dr. Waranont Anukool)

10 July 2015

To

My Family

ACKNOWLEDGEMENT

It is a genuine pleasure to express me deep sense of thanks and gratitude to all those who give me the possibility to complete this thesis. I would like to express my gratitude to my supervisor, Dr. Waranont Anukool, for his supervision, encouragement, wise suggestion, and all kind helps all the time of research. This study could not be done without close support from all members of Quantum Atom Optics Laboratory, especially Dr. Narupon Chattrapiban, N. Tanasanchai, and K. Srakowl for exchanging ideas and experiences on this research. I gratefully acknowledge Development and Promotion of Science and Technology Talent Project (DPST) for all supports. Finally, it is a pleasure to express my gratitude wholeheartedly to everyone whose support me to complete this work.

Rattakorn Kaewuam

Thesis Title Improvement of Single-atom Loading Efficiency Using Rydberg State

Author Mr. Rattakorn Kaewuam

Degree Master of Science in Physics

Advisor Dr. Waranont Anukool

ABSTRACT (in Thai)

A system of scalable single atom source on demand is a strong candidate for implementation of quantum computers. We purpose a mechanism for near deterministic preparation of a single atom in an optical dipole trap by combining two-photon transitions pertaining to molecular Rydberg states and blue-detuned light-assisted collisions. The molecular states were investigated using the Coulomb Green's function method. Toward a practical path to Rydberg-assisted single-atom loading, the experimental investigation of usable repulsive interaction between a Rydberg atom and a ground state atom is present. It is obtained from the measurement of light-induced trap loss in one-dimensional optical lattice.

Thesis Title	Improvement of Single-atom Loading Efficiency Using Rydberg State
Author	Mr. Rattakorn Kaewuam
Degree	Master of Science (Physics)
Advisor	Dr. Waranont Anukool

ABSTRACT

A system of scalable single atom source on demand is a strong candidate for implementation of quantum computers. We purpose a mechanism for near deterministic preparation of a single atom in an optical dipole trap by combining two-photon transitions pertaining to molecular Rydberg states and blue-detuned light-assisted collisions. The molecular states were investigated using the Coulomb Green's function method. Toward a practical path to Rydberg-assisted single-atom loading, the experimental investigation of usable repulsive interaction between a Rydberg atom and a ground state atom is present. It is obtained from the measurement of light-induced trap loss in one-dimensional optical lattice.

CONTENTS

LIST OF FIGURES

Page

CHAPTER 1

Introduction

1.1 Motivation

Linear nature of quantum mechanical world implies that all eigenstates can be manipulated, i.e. by a quantum logic gate, at the same time. Such massive quantum parallelism would enable a quantum processor to perform a large number of calculations simultaneously. In consequence of the superposition, the quantum bits (qubits) can do things that ordinary bits cannot. Since all eigenstates encoded into a quantum register are coherent, suitable quantum algorithms could exploit the quantum interference and delayed measurements to observe the weights cancellation that leaves only a very small number of calculated answers. For a few repeated computations, the distribution of informative outcomes pertaining to all parallel inputs would lead to an exponential speedup over classical computers.

Although the capabilities of a quantum processor to harness laws of quantum mechanics are exceptionally appreciated in the theoretical point of view, viable technologies are facing practical problems in preparing a robust multiple-qubit composite that satisfies the DiVincenzo criteria [1]. Nearly three decades have passed since the universal quantum computer was first proposed [2], several efficient and promising candidates for such physical system are still under investigations [3]. Among those approaches, trapped neutral atoms provide a number of attractive features, e.g. weak interaction with neighbors and the ability to initialize all qubits in a simple fiducial state, which make them outstanding for controlling quantum decoherence.

Along the pathway of using cold neutral atoms, the realization of quantum computer strongly depends on the specific preparing techniques and the method for coupling single atoms. In addition to the standard Doppler cooling techniques [4–6], the trapped atoms can be further cooled to the motional ground state of the potential wells [7], and their

electronic states can be prepared in a desired quantum state using standard techniques of optical pumping [8]. The electronic, spin and motional (oscillation and translation) states provide degrees of freedom for defining unique qubits. The optical trap itself and external fields make available a variety of manipulations for coherent control of such states. Making all these to a profitable account inherently directs to the most widely studied trapping technology, the optical lattices [9] is an artificial periodic potentials of light that can store cold atoms as a crystal and also open innovative manipulation possibilities such as parallel operations in a quantum computer. Fig.(1.1) shows an illustrative model of optical lattices.

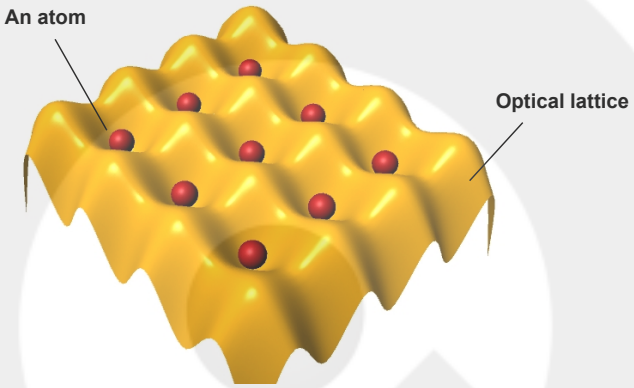

Figure 1.1: Optical lattice potentials (yellow) formed by superposition of orthogonal standing waves. The lattice can be approximated by array of harmonic oscillator potentials at each lattice site where an atom (red sphere) can be trapped.

To perfectly imitate a crystal, the ability to deterministically fill each optical well with an atom, hence qubits, is fundamentally crucial. Since the physics of each individual optical lattice site is the same as that of an optical microtrap, mastering the technique for efficient loading of a single atom in a far off-resonant dipole trap would implement scalable quantum computing as desired.

In the past 20 years, few techniques ranging from microscopic magnetic trap [10,11] to optical dipole trap [12–14] and two-dimensional optical lattices loaded from Bose-Einstein condensate [15] have been introduced to pave the way for single atoms on demand. Once believed to be limited at 50% loading probability based on the sub-

Poissonian scheme that relies on collision blockade regime [16], delicately engineering bimolecular structure and controllable interactions with light has enabled process repetition along a forced path, accumulating the chance for particular outcome. Recently by precisely blue-detuning the collision beam from the repulsive semi-molecular potential, such parametrical optimization has proven to increase the trap efficiency to 82.7% [17, 18].

According to the latest work on single atom loading an optical microtrap based on the blue-detuned light-assisted cold collision, the efficiency of 91% has been achieved. However, besides the well designed experiment, the statistical loading does not come close to the determinism demanded for optical lattices due to the lack of control over crucial parameters, such as kinetic energy shared, actual trap depth and trap geometry. To increase the probability of confining a single atom, the physical process underlying the loading mechanism should not strongly depends on probabilistic of sharing kinetic energy and those partially uncontrollable parameters. Various alternative techniques concerning the preparation of a single atom by using highly excited Rubidium atom, the Rydberg atom, have been investigated of which only two considerable processes are given here.

1. Switching the red-detuned dipole trap to blue-detuned one with similar spatial intensity distribution to kick all ground state atoms out of the trap.

2. Chirping the frequency of Rydberg excitation beam from the side of the optical micro trap towards the center. While cold ground state atoms are trapped at the center, the hot atoms on the potential edge are excited to a long-live Rydberg state and will be either springed away by atomic collisions or pushed out by repulsive dipole force.

The first approach has introduced so many experimental difficulties with questions of scalability. For example, the ability to excite one Rydberg atom at a time, the Rydberg atom lifetime to confine the time scale for color switching red→blue then blue→red again in order to finally have the ground state atom, the sensitivity to the optical alignment of overlap trap beams etc.

On the other hand, the second approach has led to theoretical investigation and experimental verification in this work. Fundamental questions immediately arose, i.e. how to eliminate the loss probability of the last atom occasionally excited to the atomic Rydberg state and how to suppress the ground state atom losses due to simultaneous and pairwise collisions with the same Rydberg atom. Though the solutions can be promptly given without any affirmative calculation, i.e. by using two-photon excitation and small principal quantum number respectively without any frequency chirping required, the realization of Rydberg Springer relies on several other behaviors that require intensive calculations. For example, what is the appropriate adiabatic repulsive potential curve? Does it really exist? How much light shift of Rydberg states? and how long does the Rydberg molecular state live? Even though the path to Rydberg Springer was beyond the compass at the beginning, the advantages of the Rydberg assisted single atom trap over the standard light-assisted technique [2] that has been the driving force for further explication throughout the rest of this thesis can still be deduced as shown in Table 1.1.

Table 1.1: The comparison between Rydberg springer approach and the blue-detuned light-assisted collisions [17, 18] that holds the world record of 91% loading efficiency.

Rydberg springer	**Light-assisted collision**
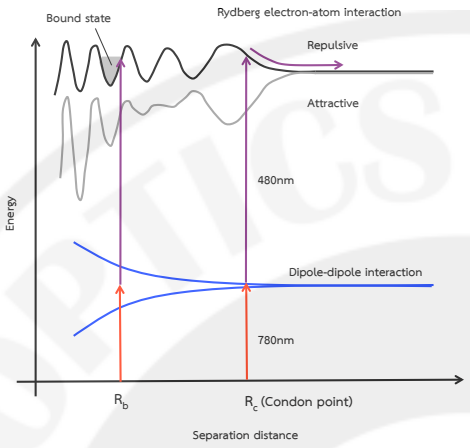	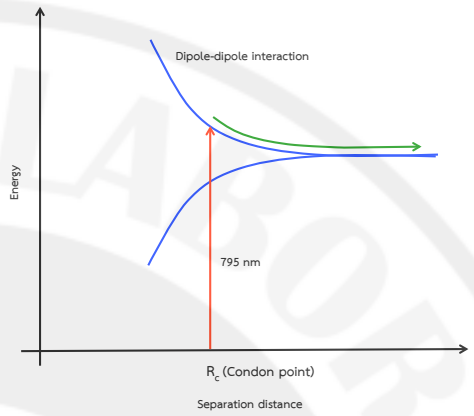
Main concept: Lifetime of Rydberg state	Main concept: Kinetic energy share
1. It does not need the large blue detune, that may induces two-atom loss event, because the lifetime of Rydberg atom play the crucial role in one-atom loss instead of statistical sharing of the kinetic energy. Detuning far from the transition line width that can prevent the last trapped atom from the optical excitations is the only requirement.	1. It requires large blue detuning compared to trap depth that can cause two-atom loss at a collision.
2. High probability of one-body loss per collision is expected.	2. It requires many collision events before single atom loss event takes place.
3. The overall performance does not strongly depend on trap depth.	3. The performance strongly depends on trap depth and specific to an experiment.
4. Need fine tuning on the two-photon transition.	4. Single photon transition is of main concern.

5. The probability of excitation to metastable bound states must be minimized	5. Blue detune can easily avoid bound state.
Advantages 1. Insensitive to trap size or geometry. Only require minimum depth and local bound state. 2. All uncontrollable parameters, e.g. energy shared between collision pair, do not determine the single atom loss event or loading efficiency. 3. As long as blue-detuning is small compared with trap depth, the mechanism is insensitive to the amount of blue-detuning.	**Disadvantages** 1. The key control, kinetic energy shared, is uncontrollable in a collision event. 2. Amount of blue-detuning plays the key role of maximum energy gained. But what reduces the loading probability is the trap itself. 3. The precisely measured depth of the dipole trap (relative to the temperature of the trapped atoms) strongly determines the single atom loss event. 4. The approximation of Gaussian trap only good at far-detuning and high beam intensity limit. Otherwise the trap geometry is not represented by the spatial distribution of the dipole beam. This is also crucial for loss events. 5. The question of scalability to optical lattices which is hard to make all potential wells identical arises.

In this work, a mechanism for determinism of single-atom loading is proposed to be achievable via a forced path that combines the two-photon excitation of molecular Rydberg states [19] and the blue-detuned light-assisted collision [20]. The mechanism relies on the fact that i) the dipole force from a red-detuned optical dipole trap or an

optical lattice usually pins the cold ground state atoms at the bottom of the trap while appeared weakly repulsive to the Rydberg ones [21] and ii) Rydberg states have very long radiative lifetime. When a colliding atomic pair is excited to a repulsive semi-molecular potential between Rydberg atom and ground-state atom, the two atoms repel from each other and only the Rydberg atom has a chance for exiting the trap due to no confining force exerting on it. If this one-body collisional loss is induced for many times, there are eventually only two atoms left in the trap. Similar collisional process would force one atom to stay in the ground state and the other, the Rydberg one, always escapes no matter what the relative velocities of the two cold atoms with respect to the trap. Therefore, the final outcome could be that there is only one atom remaining in the trap.

In addition to theoretical calculation of a semi-molecular potential appropriated for single-atom loading mechanism, this work also presents the experimental investigation of repulsive interaction between two rubidium atoms excited to a molecular Rydberg state. The signature of usable repulsive potential was explored through measured trap loss in one-dimensional optical lattice due to blue-detuned two-photon excitation.

1.2 Thesis outline

This thesis consists of three years of work carried out to map out systematic operations and explore an idea of exploiting the adiabatic energy levels of Rydberg states of Rb_2 to improve single-atom loading efficiency in an optical dipole trap. The structure of this thesis is as following.

Chapter 2 is an overview about basic concepts of laser cooling and trapping techniques including magneto-optical trap, optical dipole trap and optical lattice. These concepts of atom-light interactions are frequently mentioned throughout the thesis. The theoretical background necessary for the development of our single-atom loading mechanism is also explicated. It includes i) theoretical model of long-range interaction potential of molecular Rydberg state of Rb_2, ii) stimulated two-photon transition, and iii) blue-detuned light-assisted cold collision.

Chapter 3 presents our purposed mechanism that utilizes the repulsive interaction

potential of Rb_2 in a Rydberg state to increase the probability for single-atom loading in an optical dipole trap. The experimental conditions for achieving a near-deterministic single-atom loading process was suggested and discussed in this chapter.

Chapter 4 details the experiment and results of light-induced trap loss measurement chosen for testing the possibility of the single-atom loading mechanism using Rydberg state. The data presented in this chapter were collected from the Centre for Quantum Technologies (CQT), Singapore.

CHAPTER 2

Theoretical Background

This work mainly concerns about the utilization of molecular Rydberg state of Rb_2 to improve the single-atom loading efficiency in an optical trap. Since all physical phenomena related to this work happen under low temperature regime, vary from μK to mK, physics of laser cooling and trapping are important. The thermal atoms must undergo a series of cooling processes in order to reach the sufficiently low temperature such that it can be trapped in an optical trap. Section 2.1 and 2.2 give an overview of standard cooling and trapping techniques used in this thesis. Rydberg atom and its general properties are introduced in section 2.3. Section 2.4 focuses on the quantum mechanical formulation of two interacting atoms consisting of a Rydberg atom and a ground-state atom. This system plays a crucial role in development of our single-atom loading mechanism. Due to the excitation of molecular Rydberg state of Rb_2 requires two-photon transition driven by 780 nm and 480 nm light, section 2.5 gives a general description of two-photon excitation and dynamic of multilevel atom in light fields. Section 2.6 presents a theoretical model of light-assisted cold collision in blue-detuning regime. The model is used to evaluate the possibility and conditions for achieving deterministic single-atom loading.

2.1 Magneto-optical trap (MOT)

MOT is a standard technique that is widely used to cool thermal atoms from a room temperature to around hundreds of μK and confining the atoms in a particular region. The central concept of cooling atoms using MOT is that of the scattering force [22]. The origin of scattering force arise from atoms absorb photons and then momentum of photon is transferred to the atoms. For every absorbed photon, the atom receives a momentum change in the direction of photon propagation. The change of momentum due to spontaneous emission will be in random directions, hence its average change becomes zero.

Assuming an atom is a two-level system, the scattering force exerting on the atom in the presence of a laser field having wavelength of λ is given by [Ref]

$$F_{sp} = \hbar\pi\frac{\gamma}{\lambda}\left(\frac{s_o}{1+s_o+(2\Delta/\gamma)^2}\right), \tag{2.1}$$

where γ is natural decay rate, s_o is the saturation parameter, and Δ is the detuning from atomic transition. This force can be used to slow atoms by tuning frequency of laser below the transition frequency. This can be called the light is red-detuned from atomic transition. If the atom moves in a direction opposite to the beam propagation, it experience a Doppler shift that will bring the frequency of laser close to transition frequency, hence Δ is reduced and the force F_{sp} increased. The speed of atom slow down since the direction of force is opposite to the direction of atom's motion.

Spatial confinement of MOT is possible using a pair of anti-Helmhotz coils to produce a radial magnetic field gradient and three pairs of red-detuned circularly polarized, counter-propagating and counter-polarized beams. The three pairs are intersect at perpendicular angles at the point where the magnetic field is zero. Fig.(2.1) shows the illustrative optical alignment of MOT. By assuming the two-level atom has angular momentum quantum number $J = 0$ for ground state and $J = 1$ for excited state, the tapping scheme of MOT can be described as follow. Near the origin point where magnetic field is zero, the radial magnetic field $B(r)$ increases linearly, hence the Zeeman shift of sub-magnetic levels m_J are position dependent,

$$\Delta E_Z = \frac{\mu_B}{\hbar}\frac{dB}{dr}r, \tag{2.2}$$

where μ_B is the Zeeman constant and dB/dr is the magnetic field gradient in radial direction. The Zeeman shifts are shown in Fig.(2.2). It is clear that an atom moving along positive position will scatter σ^+ photons at a faster rate than σ^- photons because the Zeeman effect will shift the magnetic sub-level $m_J = +1$ down and the transition frequency closer to the light frequency (purple arrow). Consequently the atom experience imbalanced force that the net force directs to the center of trap. The same description

can be applied where the atom moves along negative position. Therefore the position dependent force acts as restoring force exerting on the atom. The total force acting on the atom is

$$F_{MOT} = -\alpha \frac{dr}{dt} - Kr, \tag{2.3}$$

where the first term on RHS is the damping force due to Doppler effect and the second term is the restoring force due to position-dependent of Zeeman effect. The damping constant α and the spring constant K are given by

$$\alpha = -4\hbar k^2 s_o \left(\frac{2\Delta/\gamma}{1 + (2\Delta/\gamma)^2} \right), \tag{2.4}$$

and

$$K = \frac{\alpha}{k} \frac{\mu_B}{\hbar} \frac{dB}{dr}, \tag{2.5}$$

where k is the wavenumber of laser.

So far the two-level system is used to describe the operation of MOT. In a real situation where atom is a multi-level atom, the excitation scheme becomes more complicated. Theoretically, cooling and trapping of rubidium-87 atoms using MOT can be achieved only via the cyclic transition $F = 2 \rightarrow F' = 3$ of the D2 line. However, the existence of non-zero line width and multi energy levels causes atom loss from the cyclic transition. Let a rubidium atom is in the hyperfine ground state $F = 2$. Although the frequency of laser may be red-detuned to fall between $F' = 2$ and $F' = 3$ so that the transition rates for $F = 2 \rightarrow F' = 1$ and $F = 2 \rightarrow F' = 2$ are small compared to $F = 2 \rightarrow F' = 3$, such small excitation rates can lead to a loss of atoms from the cooling cycle caused by spontaneous emission to the other ground state, i.e. $F' = 3 \rightarrow F = 2$. Since the splitting between the two ground states ($F = 1$ and $F = 2$ for Rubidium 87) is very large, about 6.8GHz, atoms confined in this ground state are no longer cooled and trapped. In order to survive efficient cooling and trapping, a second laser beam, called repumping beam, was used to pump atoms from the avoid ground state ($F = 1$) recaptured back to the cyclic ground state ($F = 2$).

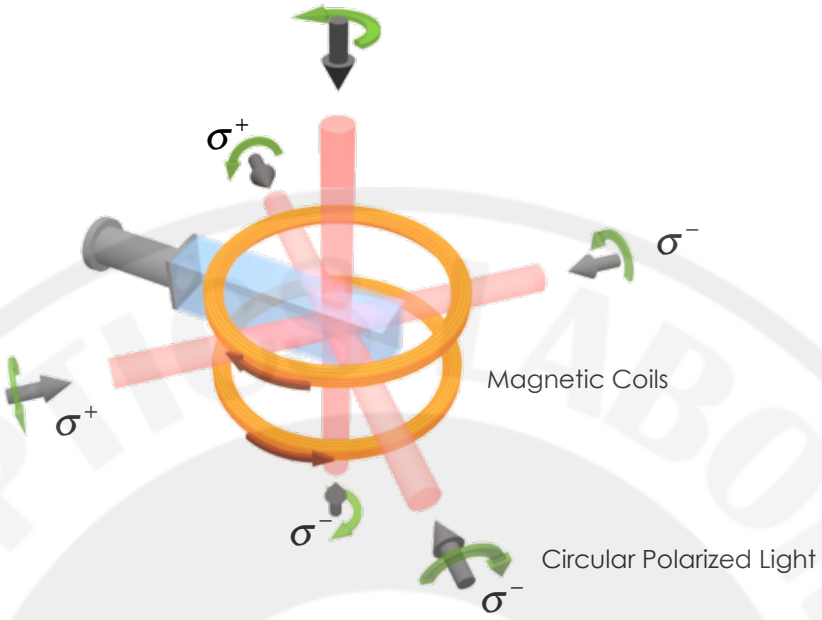

Figure 2.1: Optical alignment of magneto-optical trap.

2.2 Optical dipole trap and optical lattice

An optical dipole trap [23] confines atoms by generating the spatial gradient of energy light shift induced by a far-detuned laser light field that perturbs electronic could of an atom. The nature of dipole force is conservative and proportional to the gradient of the optical intensity. Hence it can be mathematically represented in term of a potential. The perturbation of a far-detuned laser light on a multilevel atom can be treated as a second order perturbation. The light shift of a particular state $|i\rangle$ can be written as

$$\Delta E_i = \sum_{j \neq i} \frac{|\langle j| \hat{\boldsymbol{H}}_I |i\rangle|^2}{E_i - E_j} \tag{2.6}$$

where $\hat{\boldsymbol{H}}_I$ is the interaction Hamiltonian that has the form as

$$\hat{\boldsymbol{H}}_I = \vec{\mu} \cdot \vec{E} \tag{2.7}$$

where $\vec{\mu}$ and $\vec{E}$ are dipole moment of atom and electric field of light respectively.

An illustrative picture of 1D optical lattice is shown in Fig.(2.3). The standing-

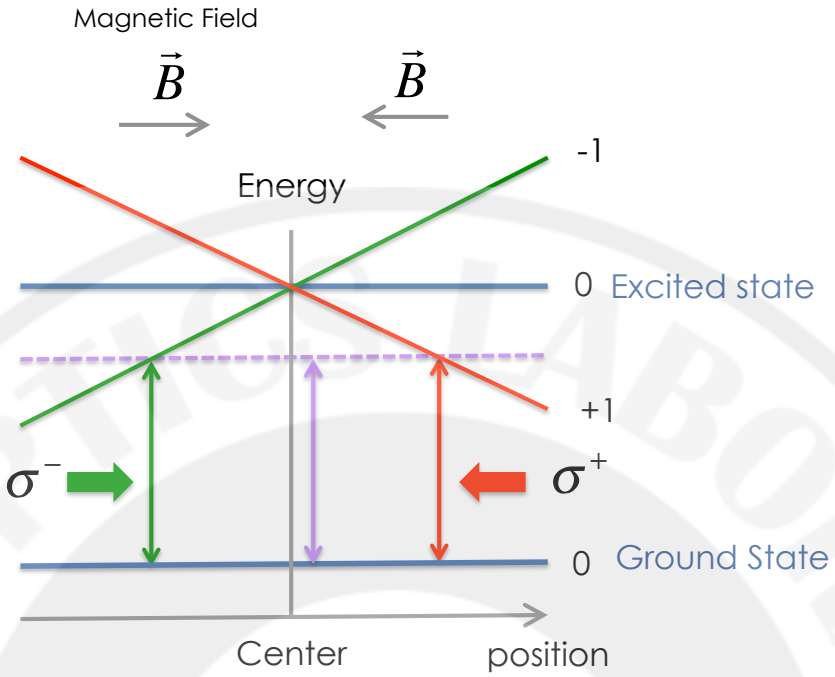

Figure 2.2: Principle of MOT

wave interference pattern creates a periodic potential inside an optical cavity formed by two cavity mirrors. Assuming TM_{00} mode where the spatial profile of the standing wave is Gaussian and letting the wavelength λ of dipole laser is very long compared to the transition wavelengths of atoms, the corresponding trap potential is written in cylindrical coordinated as,

$$U(r,\phi,z) = U_o(z)\exp\left(-\frac{2r^2}{w(z)^2}\right)\cos^2\left(\frac{2\pi}{\lambda}z\right) \tag{2.8}$$

where the trap depth $U_o(z)$ is set to be negative value and a function of position along the cavity axis $\hat{z}$. The z-dependence of U_o comes from the fact that the intensity of laser beam has different values at different position z. Here $z = 0$ means the center between the two mirrors. $w(z)$ is the beam radius of the Gaussian beam at a particular z.

2.3 Rydberg atoms

Rydberg states of an atom are defined as the electronic states that have high principle quantum number n in which its valence electron is loosely bound at a large distance from the ion core. Many behaviors and characteristics of Rydberg atoms have been

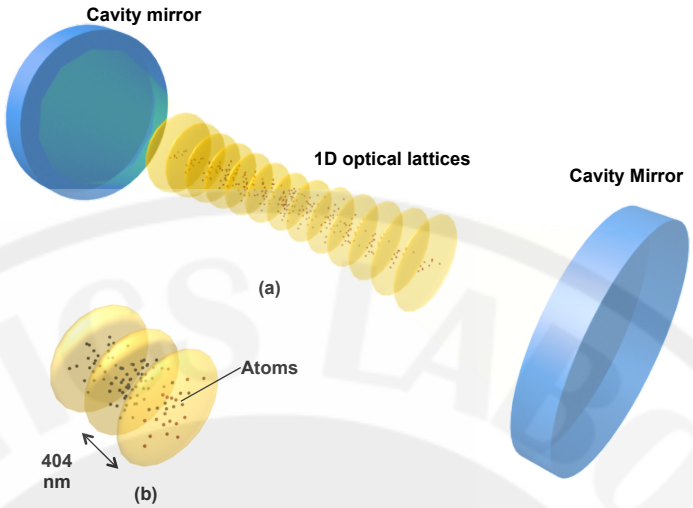

Figure 2.3: An one-dimensional optical lattice can be formed between two mirrors. Atoms are confined at anti-nodes (yellow pancake-like shape) of the standing wave. Any two adjacent sites are separated by the haft of dipole laser wavelength, here 808 nm laser is used. The picture is not drawn with true scale.

studied using the quantum defect theory [24]. General properties of Rydberg atom are very small binding energy, very long radiative lifetime [25] (vary from tens to hundreds microseconds), large dipole matrix element [26], and very sensitive to external electric field [27]. Theses atoms also exhibit strong long-range dipole-dipole interaction at distances and we proposed that it would provide deterministically a single-atom loading in an optical dipole trap.

2.3.1 Quantum Defect

According to the quantum defect theory, the energy levels of a quantum state $|n\ell j\rangle$ of an alkali atom appear as the distortion from energy levels of hydrogen atom in term of effective principle quantum number n_{eff}

$$E_{n\ell j} = -\frac{1}{2(n-\delta_{\ell j})^2} = -\frac{1}{2n_{\text{eff}}^2}, \tag{2.9}$$

Table 2.1: The quantum defect constant

Parameter	$nS_{1/2}$	$nP_{1/2}$	$nP_{3/2}$	$nD_{3/2}$	$nD_{5/2}$
δ_o	3.1311804	2.6548849	2.6416737	1.3480917	1.34646572
δ_2	0.1784	0.2900	0.2950	-0.6028	-0.5860

where n is principle quantum number and $\delta_{n\ell j}$ is called quantum defect calculated from the expression

$$\delta_{n\ell j} = \delta_o + \frac{\delta_2}{(n-\delta_o)^2}, \tag{2.10}$$

where δ_o and δ_2 are parameters obtained from fitting the measured transition energies. Mathematically, the term quantum defect δ is defined as a small defection of principle quantum number n from hydrogen atom. The origin of the defection arises from the finite size of the ionic core of the alkali atom, which for rubidium, it consists of the nucleus and 36 electrons. For low-ℓ, the valence electron penetrates into the ionic core and hence polarizes the core. The wave functions and eigenenergies of the alkali metals are modified by the interaction between nucleus and the valence electron. The experimental quantum defect constants of rubidium atom are listed in table 2.1.

2.3.2 Radiative lifetime of Rydberg states

The zero-Kelvin radiative lifetimes of Rydberg state is normally described by using a simple analytical expression of the form

$$\tau_o = \tau_R {n_{\text{eff}}}^{\epsilon} \tag{2.11}$$

where τ_R and ϵ are constants found by fitting the calculated τ_o values as a function of the effective principal quantum number n_{eff}. Values for τ_R and ϵ reported in [25] are given in table 2.2. Fig.(2.4) shows the plot of zero-Kelvin radiative lifetime of Rydberg states $nS_{1/2}$ and $nD_{3/2,5/2}$ calculated from Eq.(2.11).

Table 2.2: Values of the parameters τ_R and ϵ in Eq.(2.11)

Parameter	$nS_{1/2}$	$nP_{1/2}$	$nP_{3/2}$	$nD_{3/2}$	$nD_{5/2}$	validity range
τ_R	1.368	2.4360	2.5341	1.0761	1.0687	$10 < n < 80$
ϵ	3.0008	2.9989	3.0019	2.9898	2.9897	

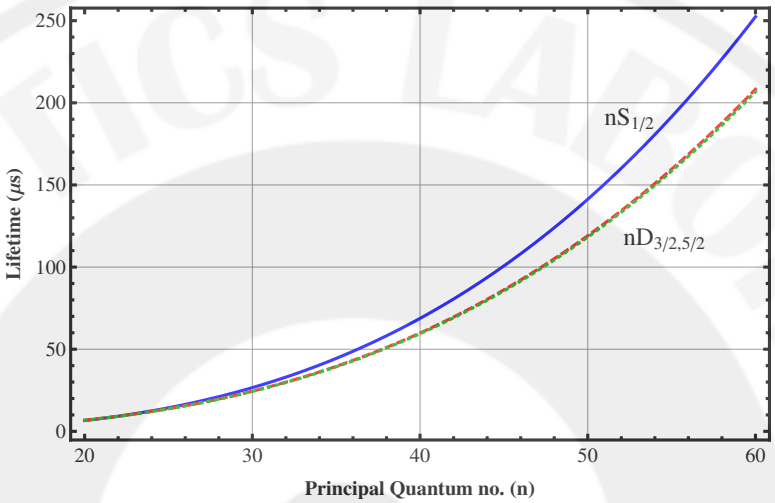

Figure 2.4: Lifetime of Rydberg state $nS_{1/2}$ (blue), $nD_{3/2}$ (dashed Red) and $nD_{5/2}$ (dotted Green) as function of principle quantum number n.

2.4 Rydberg-ground adiabatic interaction

Molecular Rydberg states play an important role in our proposed single atom loading mechanism in an optical dipole trap, section 3.1. In an experimental point of view, it is necessary to know about strength of Rydberg-ground interaction. This section presents the theoretical study of interaction between a Rydberg atom and a neutral ground-state atom. The theoretical approach and the concept of calculation method presented here follow Khuskivadze's work [28]. The adiabatic picture is exploited by assuming that relative velocity of colliding atomic pair to be much lower than velocity of Rydberg electron. This allows the application of Born-Oppenheimer approximation for the potential energy curves calculation.

Table 2.3: The fit parameters in atomic unit for the pseudopotential $V_{LS}(r)$ in Eq.(2.64) and Eq.(2.65) [28].

α	λ	State	A	γ	r_c
319.2	7.4975	^1S	4.5642	1.3438	1.8883
		^3S	68.576	9.9898	2.3813
		^1P	-4.2625	1.0055	1.8869
		^3P	-1.4523	4.8733	1.8160

2.4.1 Formalism

The system consists of a Rydberg ion core C^+, a neutral alkali ground-state atom B, and a Rydberg electron e^-, Fig. 2.5. The whole position space is divided into two hard physics regions: The region *I* where the e-B interaction (inside the sphere of radius r_0) dominated and the region *II* dominated by the e-C^+ interaction (space enclosed by surfaces S_1 and S_2). The interaction in region *I* is taken into account by utilizing the Coulomb's Green function including quantum defect [29, 30]. Due to the nature of screening effect, the e^--B interaction mainly results from the Rydberg electron interacting with the valence electron of the neutral atom B and it can be represented in term of short-range pseudopotential [31]. Hence the angular momentum basis set is chosen to be $\{L, S, J, M_J\}$ where L, S, and J are two-electron orbital angular momentum, two-electron spin, and total angular momentum respectively. Since the problem has a cylindrical symmetry along the internuclear axis $\vec{R}$, the projection of total angular momentum j on the axis is a constant of motion, hence M_J is conserved. In the Born-Oppenheimer approximation, one can consider the Hamiltonian of the Rydberg electron interacting with C^+ and B, and the Hamiltonian of C^+-B separately. For the first case, the corresponding Schrödinger equation in atomic unit of the single Rydberg electron in the presence of the neutral atom B and its ion core C^+ is

$$\left(-\frac{1}{2}\nabla^2 + \hat{V}_I(\vec{r},\vec{R}) - \frac{1}{|\vec{r}-\vec{R}|} + V_{qd}(\vec{r}-\vec{R})\right)\Phi_{M_J}(\vec{r},\vec{R}) = E_{M_J}\Phi_{M_J}(\vec{r},\vec{R}), \quad (2.12)$$

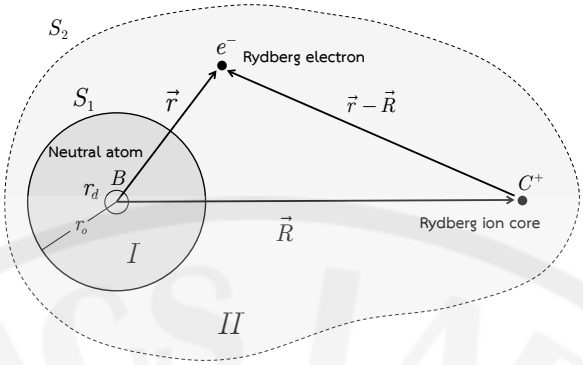

Figure 2.5: Coordinate system used in this work. The position of atom B is chosen to be the origin. The internuclear $\vec{R}$ is a vector directed form neutral atom B to the core C^+ of Rydberg atom. It is the quantization axis. $\vec{r}$ is a position vector pointed from neutral atom B to the valence electron e. r_0 is the radius of the sphere enclosed by surface S_1 dividing space into two region where the closed sufrace S_2 extends to infinity.

where the subscript M_J means that it is a good quantum number that can be used to specify an eigenstate Φ_{M_J}. The interaction potential $\hat{V}_I(\vec{r},\vec{R})$ is given by

$$\hat{V}_I(\vec{r},\vec{R}) = V_{eB}(\vec{r}) - \frac{\alpha_o \vec{r}\cdot\vec{R}}{r^3R^3}. \tag{2.13}$$

The first term of Eq.(2.13) is the combination of the spin-orbit interaction and the short-range pseudopotential of e-B that reproduces the electron binding energies for negative ion and the scattering phase shifts given by the Dirac *R*-matrix calculation [32]. The second term is the effect of three-body polarization interaction consisting of the neutral atom B polarized by the ion core C^+ interacts with the Rydberg electron e^-, and the atom B polarized by e^- interacts with the ion core C^+. The polarizability α_o of a neutral rubidium atom is given in [33]. The third and the fourth terms of Eq.(2.12) describe the Coulomb interaction and the quantum defect correction respectively. All interaction described so far are only about Rydberg electron interacting with the neutral atom and its ion core. To obtain the total energy of the interacting system C+B, it is needed to add C^+-B polarization interaction to the electron energy E_{M_J}

$$U_{M_J}(R) = E_{M_J} - \frac{\alpha_o}{2R^4}. \tag{2.14}$$

In order to find an eigenenergy of the Schrödinger equation Eq.(2.12), it is necessary to compose appropriate boundary conditions of the surface S_1 and S_2 on the Eq.(2.12) and then solve the differential equations. Due to the Coulomb interaction dominates in outer region *II* and its range is infinite, the wave function Φ_{M_J} vanishes on the surface S_2 that extends to infinity. The boundary condition on S_1 is related to the way of matching wave functions having different symmetries (spherical and cylindrical) in the two regions of space. Khuskivadze [28] have done well this matching by using the Kirchhoff-integral method in term of Coulomb Green function [34]. He matches the inner wave function with the outer wave function on the surface S_1 using the Kirchhoff integral equation. It allows him to incorporate the boundary conditions at infinity where the wave function decays exponentially. In this work, the derivation of the Kirchhoff integral equation is presented in the slightly different way. The quantum Coulomb Green's function $G_R(\vec{r}, \vec{r}\,', E_{M_J})$ is defined as the solution of the Coulomb Schrödinger equation where there is a point source placed at $\vec{r}\,'$,

$$\left(-\frac{1}{2}\nabla^2 - \frac{1}{|\vec{r}-\vec{R}|} + V_{qd}(\vec{r}-\vec{R}) - E_{M_J}\right) G_R(\vec{r}, \vec{r}\,', E_{M_J}) = -\delta(\vec{r}-\vec{r}\,'), \qquad (2.15)$$

where $G_R(\vec{r}, \vec{r}\,', E_{M_J}) \equiv G(\vec{r}-\vec{R}, \vec{r}\,'-\vec{R}, E_{M_J})$ is the Green funcstion whoes center is shifted to be at $\vec{R}$. By multipying Eq. (2.12) by $G_R(\vec{r}, \vec{r}\,', E_{M_J})$, Eq. (2.15) by $\Phi_{M_J}(\vec{r}, \vec{R})$, then substracting one from another and take volume integration over space inside the sphere of radius r_o, the result is

$$\frac{1}{2}\int_{\mathrm{V_1}} \left(\Phi_{M_J}\nabla^2 G_R - G_R\nabla^2\Phi_{M_J}\right) d^3\vec{r} + \int_{\mathrm{V_1}} \hat{V}_I G_R \Phi_{M_J} d^3\vec{r} = \Phi_{M_J}(\vec{r}\,', \vec{R}). \qquad (2.16)$$

The equation is valid if $0 < r' < r_o$. After using the Green's second identity to transform the volume integral to the surface integral for the first term which contains kinetic energy operator ∇^2,

$$\frac{1}{2}\oint_{\mathrm{S_1}} \left(\Phi_{M_J}\nabla G_R - G_R\nabla\Phi_{M_J}\right)\cdot d\mathbf{S} + \int_{\mathrm{V_1}} \hat{V}_I G_R \Phi_{M_J} d^3\vec{r} = \Phi_{M_J}(\vec{r}\,', \vec{R}), \qquad (2.17)$$

where $d\mathbf{S}$ is the normal vector on S_1 and V_1 is the volume inside the sphere of radius r_o enclosed by the surface S_1. According to the scattering theory in the framework of quantum mechanics, the corresponding Lippman-Schwinger equation [35] is

$$\Phi_{M_J}(\vec{r}\,', \vec{R}) = \phi_0(\vec{r}\,', \vec{R}) + \int \hat{V}_I(\vec{r}, \vec{R}) G_R(\vec{r}, \vec{r}\,', E_{M_J}) \Phi_{M_J}(\vec{r}, \vec{R}) d^3\vec{r}, \tag{2.18}$$

where the wave function $\phi_0(\vec{r})$ is an eigenfunction of non-perturbed Rydberg atom. This eigenfunction is chosen to vanish because the system of perturbed Rydberg atom is been considering. Notice that the second term of Eq.(2.18) is the integral over all space. However if the radius r_0 is larger than the effective radius of potential $\hat{V}_I$, the infinite integral can be transformed to be a finite integral over the region inside the sphere of radius r_0. Hence, from Eq. (2.17) and Eq. (2.18),

$$\oint_{S_1} (\Phi_{M_J} \nabla G_R - G_R \nabla \Phi_{M_J}) \cdot d\mathbf{S} = 0 \qquad : 0 < r' < r_0. \tag{2.19}$$

This is the same result presented in [28,34,36] and it is called *Kirchhoff-integral equation*. It can be used as a matching condition for wave functions on the surface S_1. Hence it is an equation for determination of the eigenenergies.

In order to utilize the spirit of Eq. (2.19), it is needed to transform the integral equation into a particular form that the calculation can be performed numerically. The transformation is done by expanding Eq.(2.12) on the angular momentum basis set $|\alpha\rangle$. The short-range e-B interaction potential can be written in the form of pseudopotential as

$$\hat{V}_{eB}(\vec{r}) = \sum_{\alpha} F_\alpha(r) \left|\alpha\right\rangle \left\langle\alpha\right|, \tag{2.20}$$

where the summation is taken over angular momentum of two-electron spinor in L-S coupling scheme, $\alpha = \{L, S, J, M_J\}$. $F_\alpha(r)$ is a combination of the effective interaction of an electron and a neutral atom plus the spin-orbit interaction

$$F_{LS}(r) = V_{LS}(r) + \frac{1}{2c^2 r} \frac{dV_{LS}}{dr} (\vec{\boldsymbol{\ell}}_{\mathbf{1}} \cdot \vec{\boldsymbol{s}}_{\mathbf{1}}), \tag{2.21}$$

where $\vec{\boldsymbol{\ell}}_{\mathbf{1}} \cdot \vec{\boldsymbol{s}}_{\mathbf{1}}$ operator acts only on the Rydberg electron because it is assumed that the alkali atom B is in the ground state, hence its valence electron is in the S orbital. The pseudopotential $V_{LS}(r)$ has a spherical symmetry and its explicit form is given in subsection 2.4.3. Then the wave function $\Phi_{M_J}(\vec{R}, \vec{r})$ inside the inner region *I* is expanded in the two-electron angular momentum basis

$$\Phi_{M_J}(\vec{R}, \vec{r}) = \sum_{\alpha'} \frac{u_{\alpha'}(r)}{r} |\alpha'\rangle , \tag{2.22}$$

where $u_{\alpha'}(r)$ is the *radial* wave function and the angular momentum basis $|\alpha\rangle$ is expanded on the uncouple basis $|LM_L\rangle$ and $|SM_S\rangle$

$$|\alpha\rangle = |LSJM_J\rangle = \sum_{M_L, M_S} C^{J,M_J}_{L,M_L,S,M_S} |LM_L\rangle |SM_S\rangle , \tag{2.23}$$

where $\vec{\boldsymbol{L}} = \vec{\boldsymbol{\ell}}_{\mathbf{1}} + \vec{\boldsymbol{\ell}}_{\mathbf{2}}$, and $\vec{\boldsymbol{S}} = \vec{\boldsymbol{s}}_{\mathbf{1}} + \vec{\boldsymbol{s}}_{\mathbf{2}}$ are total orbital angular momentum and total spin of two electron. The Clebsch-Gordan coefficients C^{J,M_J}_{L,M_L,S,M_S} are given by,

$$C^{J,M_J}_{L,M_L,S,M_S} = (-1)^{-L+S-M_J} \sqrt{2J+1} \begin{pmatrix} L & S & J \\ M_L & M_S & -M_J \end{pmatrix} , \tag{2.24}$$

where $|LM_L\rangle$ are the spherical harmonics, and $|SM_S\rangle$ are the total spin states of the Rydberg electron and the valence electron. After substituting Eq. (2.22) into Eq. (2.12), neglecting the quantum defect V_{qd} due to the effect is very small in the inner region, and then projecting Eq. (2.12) on $\langle\alpha|$, the result is the system of coupled second-order differential equations

$$\left(-\frac{1}{2}\frac{d^2}{dr^2} + \frac{L(L+1)}{2r^2} + V_{LS}(r) + I_\alpha(r) - E_{M_J} \right) u_\alpha(r, R) = \sum_{\alpha'} D_{\alpha\alpha'} u_{\alpha'}(r, R), \tag{2.25}$$

where

$$D_{\alpha\alpha'} = \langle LSJM_J| \frac{1}{|\vec{r} - \vec{R}|} + \frac{\alpha_o \vec{r} \cdot \vec{R}}{r^3 R^3} |L'S'J'M_J\rangle , \tag{2.26}$$

and

$$I_\alpha(r) = \frac{1}{2c^2 r}\frac{dV_{LS}}{dr}\left\langle LSJM_J\right|\vec{\boldsymbol{\ell}}_{\mathbf{1}}\cdot\vec{\boldsymbol{s}}_{\mathbf{1}}\left|LSJM_J\right\rangle. \tag{2.27}$$

Using Eq. (2.23) and the expansion

$$\frac{1}{|\vec{r}-\vec{R}|} = \sum_{\ell=0}^{\infty}\sum_{m=-\ell}^{\ell}\frac{r_<^\ell}{r_>^{\ell+1}}\left(\frac{4\pi}{2\ell+1}\right)Y^*_{\ell m}(\hat{\boldsymbol{r}})Y_{\ell m}(\hat{\boldsymbol{R}}), \tag{2.28}$$

where z axis is chosen along internuclear axis $\vec{R}$ and due to considering in the inner region it can be set $r < R$, hence

$$\frac{1}{|\vec{r}-\vec{R}|} = \sum_{\ell=0}^{\infty}\frac{r^\ell}{R^{\ell+1}}\sqrt{\frac{4\pi}{2\ell+1}}\,Y_{\ell 0}(\hat{\boldsymbol{r}}), \tag{2.29}$$

and then the matrix element Eq. (2.26) becomes

$$\begin{aligned} D_{\alpha\alpha'} = {} & \delta_{SS'}(-1)^{-L-L'}\sqrt{(2J+1)(2J'+1)(2L+1)(2L'+1)} \\ & \times\sum_{\ell=|L-L'|}^{|L+L'|}\left(\frac{r^\ell}{R^{\ell+1}}+\frac{\alpha_d}{r^2R^2}\delta_{\ell 1}\right)\begin{pmatrix} L & \ell & L' \\ 0 & 0 & 0\end{pmatrix}B^\ell_{\alpha\alpha'} \end{aligned} \tag{2.30}$$

and

$$B^\ell_{\alpha\alpha'} = \sum_{M_L,M_S}^{M_L+M_S=M_J}(-1)^{M_L}\begin{pmatrix} L & S & J \\ M_L & M_S & -M_J\end{pmatrix}\begin{pmatrix} L & \ell & L' \\ -M_L & 0 & M_L\end{pmatrix}\begin{pmatrix} L' & S' & J' \\ M_L & M_S & -M_J\end{pmatrix} \tag{2.31}$$

where the symbols in parenthesis denote *3j* symbol coefficients. Eq.(2.25) is the coupled radial Schrödinger equation and it can be solved numerically using a standard method in electron-atom collision theory. To solve the equations, the set of linearly independent solutions needed to be calculated first and then by exploiting the boundary condition Eq.(2.19), a suitable combination of linearly independent solutions and an eigenenergy are determined. Mathematically, a general solution of the radial Schrödinger equation Eq.(2.25) consists of regular and irregular solutions at origin. However, a physical solution should be only written as a summation of linearly independent solutions regular at

origin

$$u_{\alpha'}(r,R) = \sum_j A_j \nu_{\alpha' j}(r,R), \tag{2.32}$$

where j denotes independent solutions, and A_j are constants. The matrix $\nu_{\alpha' j}$ is called *fundamental matrix* for Eq.(2.25). Note that the number of linearly independent solutions regular at origin is equal to the number of coupled differential equations. After substituting Eq.(2.22) and Eq.(2.32) into Eq.(2.19) and then projecting on $\langle\alpha|$,

$$\sum_j A_j K_{\alpha j}(E_{M_J}) = 0, \tag{2.33}$$

where

$$K_{\alpha j}(E_{M_J}) = \sum_{\alpha'} \delta_{SS'} \tag{2.34}$$

However, near the origin, the spin-orbit interaction has non-physical singularity. the Dirac equation must be applied near the origin and then calculated Dirac wave function is transformed into Schrödinger wave function in jj representation and then transform it into LS representation (Appendix B) before performing numerical integration. This process, naturally, must be repeated for varying values of the internuclear separation R in order to map out the internuclear potentials.

2.4.2 Coulomb Green function and quantum defect correction

This section presents the expression and numerical estimation of Coulomb Green's function. Consider definition of the Coulomb Green function $G(\vec{r}_1, \vec{r}_2, E)$ as,

$$\left(-\frac{1}{2}\nabla_1^2 - \frac{1}{r_1} + V_{qd}(r_1) - E\right) G(\vec{r}_1, \vec{r}_2, E) = -\delta(\vec{r}_1 - \vec{r}_2) \tag{2.35}$$

Mathematically, the solution of Eq. (2.35) can be written as in the form of an eigenfunction expansion.

$$G(\vec{r}_1, \vec{r}_2, E) = -\sum_{\ell=0}^{\infty}\sum_{m=-\ell}^{\ell}\int_0^{\infty} \frac{\phi^*_{\ell m}(k,\vec{r}_1)\phi_{\ell m}(k,\vec{r}_2)}{(k^2/2) - E} dk - \sum_{n=0}^{\infty}\sum_{\ell=0}^{\infty}\sum_{m=-\ell}^{\ell} \frac{\phi^*_{n\ell m}(\vec{r}_1)\phi_{n\ell m}(\vec{r}_2)}{E_n - E} \tag{2.36}$$

The first term is the summation and integration over the continuous spectrum of hydrogen atom. The second term is summed over the discrete spectrum. In order to include the quantum defect in calculation, the Green function $G(\vec{r}_a, \vec{r}_b, \nu)$ has two components as

$$G(\vec{r}_1, \vec{r}_2, \nu) = G_o(\vec{r}_1, \vec{r}_2, \nu) + G_{qd}(\vec{r}_1, \vec{r}_2, \nu) \tag{2.37}$$

The first term is the particular solution of inhomogeneous equation Eq. (2.35) and the second term is the solution of homogeneous equation. The *effective quantum number* v is defined by

$$\nu \equiv \frac{1}{\sqrt{-2E}} \tag{2.38}$$

The pure Coulomb Green function in closed form is given by

$$G_o(\vec{r}_1, \vec{r}_2, \nu) = -\frac{\Gamma(1-\nu)}{2\pi|\vec{r}_1 - \vec{r}_2|}\left[W_{\nu,1/2}(\alpha)\frac{\partial}{\partial\beta}M_{\nu,1/2}(\beta) - M_{\nu,1/2}(\beta)\frac{\partial}{\partial\alpha}W_{\nu,1/2}(\alpha)\right] \tag{2.39}$$

where

$$\frac{\partial}{\partial\beta}M_{\nu,1/2}(\beta) = \left(\frac{1}{2} - \frac{\nu}{\beta}\right)M_{\nu,1/2}(\beta) + \left(\frac{1+\nu}{\beta}\right)M_{1+\nu,1/2}(\beta) \tag{2.40}$$

$$\frac{\partial}{\partial\alpha}W_{\nu,1/2}(\alpha) = \left(\frac{1}{2} - \frac{\nu}{\alpha}\right)W_{\nu,1/2}(\alpha) - \frac{1}{\alpha}W_{1+\nu,1/2}(\alpha) \tag{2.41}$$

and the arguments α and β are defined as

$$\alpha \equiv \frac{1}{\nu}\left(|\vec{r}_1| + |\vec{r}_2| + |\vec{r}_1 - \vec{r}_2|\right) \tag{2.42}$$

$$\beta \equiv \frac{1}{\nu}\left(|\vec{r}_1| + |\vec{r}_2| - |\vec{r}_1 - \vec{r}_2|\right) \tag{2.43}$$

Note that $M_{k,m}(z)$ and $W_{k,m}(z)$ are *Whittaker* function of first kind and second kind respectively. They are defined as

$$M_{k,m}(z) = e^{-z/2}z^{m+1/2}{}_1\boldsymbol{F_1}(\frac{1}{2} + m - k, 1 + 2m; z) \tag{2.44}$$

$$W_{k,m}(z) = e^{-z/2}z^{m+1/2}\boldsymbol{U}(\frac{1}{2} + m - k, 1 + 2m; z) \tag{2.45}$$

where ${}_1\boldsymbol{F}_1$ and $\boldsymbol{U}$ are *confluent hypergeometric functions* of first kind and second kind. The quantum defect correction of Green function is given by

$$G_{qd}(\vec{r}_1,\vec{r}_2,\nu) = -\frac{\nu}{r_1 r_2}\sum_{\ell=0}^{\infty}\frac{\Gamma(1+\ell-\nu)}{\Gamma(1+\ell+\nu)}\frac{sin[\pi(\delta_\ell+\ell)]}{sin[\pi(\delta_\ell+\nu)]}\frac{2\ell+1}{4\pi}P_\ell(cos\gamma) \times W_{\nu,\ell+1/2}\left(\frac{2r_1}{\nu}\right)W_{\nu,\ell+1/2}\left(\frac{2r_2}{\nu}\right) \tag{2.46}$$

where γ is the angle between $\vec{r}_1$ and $\vec{r}_2$, and δ_ℓ is the ℓ dependent quantum defects. It should be noted that by combining the Coulomb Green function and the quantum defect correction the Coulomb poles in the sum Eq. (2.37) cancel out exactly. The remaining poles are determined by

$$E_{n\ell} = -\frac{1}{2(n-\delta_\ell)^2} \tag{2.47}$$

Let the coordinate system be defined as following,

$$\begin{aligned}\vec{r}_1 &\equiv \vec{r}_a - \vec{R}\\ \vec{r}_2 &\equiv \vec{r}_b - \vec{R}\end{aligned} \tag{2.48}$$

where the vector $\vec{R}$ is directed from the neutral atom to the Coulomb ion core. Hence the cosine of angle between $\vec{r}_a - \vec{R}$ and $\vec{r}_b - \vec{R}$ is given by

$$cos\gamma = \frac{(\vec{r}_a - \vec{R})\cdot(\vec{r}_b - \vec{R})}{|\vec{r}_a - \vec{R}||\vec{r}_b - \vec{R}|} \tag{2.49}$$

The matrix element of the Green function $\langle LM_L|\, G_R\, |L'M_L\rangle$ is

$$\langle LM_L|\, G_R\, |L'M_L\rangle \equiv A\int_{S_b}\int_{S_a} Y^*_{L,M_L}(\hat{\Omega}_a)G_R(\vec{r}_a,\vec{r}_b,\nu)Y_{L',M_L}(\hat{\Omega}_b)d\Omega_a d\Omega_b \tag{2.50}$$

where the subscript R denotes R-dependence of the matrix element and the constant A is

$$A = \sqrt{\frac{(2L+1)}{4\pi}\frac{(L-|M_L|)!}{(L+|M_L|)!}} \times \sqrt{\frac{(2L'+1)}{4\pi}\frac{(L'-|M_L|)!}{(L'+|M_L|)!}} \tag{2.51}$$

Due to the cylindrical symmetry, the four dimensional integration can be reduced to three dimensional integration. Letting $r_b \sim r_a = r_0$, we obtain

$$\begin{aligned}\langle LM_L|\, G_o\, |L'M_L\rangle = -A\Gamma(1-\nu)\int_0^{2\pi}\int_0^{\pi}\int_0^{\pi}\Bigg[\nu\left(\frac{1}{\alpha}-\frac{1}{\beta}\right)W_{\nu,1/2}(\alpha)M_{\nu,1/2}(\beta) \\ +\left(\frac{1+\nu}{\beta}\right)M_{1+\nu,1/2}(\beta)W_{\nu,1/2}(\alpha) \\ +\left(\frac{1}{\alpha}\right)W_{1+\nu,1/2}(\alpha)M_{\nu,1/2}(\beta)\Bigg] \\ \times\frac{P_{L'}^{|M_L|}(cos\theta_a)P_L^{|M_L|}(cos\theta_b)}{|\vec{r}_a-\vec{r}_b|}e^{iM_L\phi}sin\theta_a sin\theta_b \boldsymbol{d}\theta_a \boldsymbol{d}\theta_b \boldsymbol{d}\phi\end{aligned} \tag{2.52}$$

where α and β in this coordinate system are given by,

$$\alpha(\theta_a,\theta_b,\phi) = \frac{1}{\nu}\left(|\vec{r}_a-\vec{R}|+|\vec{r}_b-\vec{R}|+|\vec{r}_a-\vec{r}_b|\right) \tag{2.53}$$

$$\beta(\theta_a,\theta_b,\phi) = \frac{1}{\nu}\left(|\vec{r}_a-\vec{R}|+|\vec{r}_b-\vec{R}|-|\vec{r}_a-\vec{r}_b|\right) \tag{2.54}$$

where

$$|\vec{r}_a-\vec{R}| = r(\theta_a) \tag{2.55}$$

$$|\vec{r}_b-\vec{R}| = r(\theta_b) \tag{2.56}$$

$$|\vec{r}_a-\vec{r}_b| = \sqrt{2}r_0\sqrt{1-cos\gamma} \tag{2.57}$$

where $r(\theta) \equiv \sqrt{r_0^2+R^2-2r_0Rcos\theta}$. The cosine of angle γ is given by

$$cos\gamma = C(\theta_a,\theta_b)cos\phi + D(\theta_a,\theta_b) \tag{2.58}$$

where

$$C(\theta_a,\theta_b) = \frac{r_0^2 sin\theta_a sin\theta_b}{r(\theta_a)r(\theta_b)} \tag{2.59}$$

$$D(\theta_a,\theta_b) = \frac{(r_0cos\theta_a-R)(r_0cos\theta_b-R)}{r(\theta_a)r(\theta_b)} \tag{2.60}$$

For the quantum defect correction,

$$\begin{aligned}\langle LM_L|\, G_{qd}\, |L'M_L\rangle = 2\pi A\nu \sum_{\ell=0}^{5} \frac{\Gamma(1+\ell-\nu)}{\Gamma(1+\ell+\nu)} \frac{sin[\pi(\delta_\ell+\ell)]}{sin[\pi(\delta_\ell+\nu)]} \frac{2\ell+1}{4\pi} \\ \times \int_0^\pi \int_0^\pi \frac{W_{\nu,\ell+1/2}\left(\frac{2r(\theta_a)}{\nu}\right) W_{\nu,\ell+1/2}\left(\frac{2r(\theta_b)}{\nu}\right)}{r(\theta_a)r(\theta_b)} F_{\ell,M_L}(\theta_a,\theta_b) \\ \times P_{L'}^{|M_L|}(cos\theta_a) P_L^{|M_L|}(cos\theta_b) sin\theta_a sin\theta_b \boldsymbol{d}\theta_a \boldsymbol{d}\theta_b\end{aligned} \tag{2.61}$$

where $P_L^M(z)$ is the *associated Legendre* polynomial (see *Introduction to Quantum mechanics, Davis J. Griffith, 2rd edition, p136*). The summation over ℓ in quantum defect correction is limited to the first five terms because the quantum defects for high ℓ can be ignored. The functions $F_{\ell,M_L}(\theta_a,\theta_b)$ is given by

$$F_{\ell,M_L}(\theta_a,\theta_b) = \int_0^{2\pi} P_\ell(cos\gamma) e^{iM_L\phi_a} d\phi \tag{2.62}$$

where $P_\ell(z)$ is the *Legendre* polynomial.

In order to remove poles of Green function for zero searching calculation, the matrix element can be multiplied by

$$\frac{\prod_{\ell=0}^{5} sin[\pi(\delta_\ell+\nu)]}{\Gamma(1-\nu)} \tag{2.63}$$

2.4.3 Effective interaction for electron-atom scattering

The method used to describe the interaction between an electron and an alkali atom in low-energy scattering scheme is the model-potential approach [31, 37]. Due to scattering energy is low, it is naturally to ignore the scattering wave with $L > 1$ hence only s and p wave scattering are relevant. It should be noted that by separating the interaction potentials with different orbital angular momentum L, the effective interaction can be called pseudopotential. The model-potential $V_{LS}(r)$ in Eq.(2.21) for s-wave scattering, $L = 0$, has an analytic form in atomic unit as

$$V_{0S}(r) = -\frac{A}{r} e^{-\gamma r} - \frac{\alpha}{2r^4}\left(1 - e^{(r/r_c)^6}\right) \tag{2.64}$$

while for the p-wave scattering, $L = 1$, the potential is written as

$$V_{1S}(r) = -\frac{Z_c}{r}e^{-\lambda r} - Ae^{-\gamma r} - \frac{\alpha}{2r^4}\left(1 - e^{(r/r_c)^6}\right) \tag{2.65}$$

where the constants A, γ, α, and λ are fitted parameters shown in Table.2.3. Z_c is the nuclear charge, for rubidium atom it is 37. Physics of scattering between low-energy electron and an alkali atom is relevant to a virtual ^3S state and a ^3P shape resonance [38, 39]. These features play an important role in formation of long-range molecular Rydberg states. The classical description of a shape resonance in scattering is presented [40] by the projectile of incoming electron tunneling through a potential barrier due to repulsive electron-electron interaction. The electron remains within a pseudo-bound state for a while and then tunneling out from the barrier. Although there is no a classical description of a virtual state in scattering, a simple picture of the state is described as follow. As the depth of an attractive scattering potential is decreased provided there is no potential barrier, an energy level of a bound state moves through the continuum threshold to become a pseudo-bound state called virtual state [41].

2.5 Multi-level atom in light fields and two-photon transition

The semi-classical Hamiltonian of a system consisting of an multi-level atom interacting with coherent electromagnetic fields is

$$\begin{aligned} \hat{H} &= \hat{H}_0 + \hat{V}_I(t) \\ &= \sum_j E_j \left|j\right\rangle \left\langle j\right| - \sum_{i\neq j,k} \vec{\mu}_{ij} \cdot \vec{\boldsymbol{E}}_k \left|i\right\rangle \left\langle j\right| \end{aligned} \tag{2.66}$$

where the $\hat{H}_0$ denotes the field-free time-independent atomic Hamiltonian whose eigenvalues and eigenfunctions are $E_\alpha = \hbar\omega_\alpha$ and $|\alpha\rangle$ respectively. The second term, $\hat{H}_I$, is the time-dependent interaction with radiation fields of mode k. This interaction plays the important role in transition between eigenstates of atomic Hamiltonian $\hat{H}_0$. The time evolution of optical transition of multi-level atom in the presence of coherent light fields is described using the density matrix formulation. The density operator $\hat{\rho}$ of a multi-level

system in a pure state $|\Psi\rangle$ is given by

$$\hat{\rho}(t) = |\Psi(t)\rangle \langle\Psi(t)| , \tag{2.67}$$

where the state $|\Psi(t)\rangle$ can be written in the interaction picture [35] as superposition of all eigenstates of the unperturbed Hamiltonian $\hat{H}_0$.

$$|\Psi(t)\rangle = \sum_{\alpha} C_\alpha(t) |\alpha\rangle . \tag{2.68}$$

The evolution of the density operator $\hat{\rho}$ in the representation is then described by a system of equations known as the optical Bloch equations.

$$\frac{d\hat{\rho}}{dt} = \frac{i}{\hbar} \left[\hat{\rho}, \hat{V}_I(t)\right] + \hat{G}(\gamma, \hat{\rho}), \tag{2.69}$$

where $\hat{G}$ is the operator accounting for the relaxation effect due to decoherence processes. Applying the standard *rotating wave approximation*, the matrix element of interaction potential is

$$V_{ij} = \sum_k \hbar \frac{\Omega_{ij}^k}{2} e^{-i\Delta_{ij}^k t}, \tag{2.70}$$

where Ω_{ij}^k is the on-resonance *Rabi frequency* of atomic transition $i \rightarrow j$ driven by the radiation field of mode k. This frequency fundamentally represents how fast atom absorbs photon and reemit the photon via stimulated absorption and stimulated emission. The detuning $\Delta_{ij}^k = \omega_k - \omega_{ij}$ is the frequency difference between the radiation field of mode k and the transition ij.

The operator $\hat{G}$ has both diagonal and off-diagonal (coherence) elements. Assuming that all decoherence arise from the spontaneous emission. Then the diagonal elements are determined from the conservation of probability and the off-diagonal elements G_{ij} are proportional to only the spontaneous emission rate γ_{ij} of decay channel $i \rightarrow j$. The rate γ_{ij} is determined by considering the interaction of an atom with quantized electromagnetic field in free space. This phenomena corresponds with a discrete level system

coupled to a continuum states of external field. The interaction Hamiltonian is given by

$$\hat{H}_I = i \sum_k \sum_{i \neq j} \left(\frac{\hbar \omega_k}{2 \epsilon_o V} \right)^{1/2} \mu_{ij} \cdot \vec{E}_k \left[\hat{a}_k e^{i(\vec{k} \cdot \vec{r} - \omega_k t)} - \hat{a}_k^\dagger e^{-i(\vec{k} \cdot \vec{r} - \omega_k t)} \right] |i\rangle \langle j| \qquad (2.71)$$

where the summations are taken over both all field modes k and atomic transitions of interest $i \rightarrow j$. When the analytic expression of $\hat{G}$ is known, the Eq.(2.69) can be used to setup the master equations where its solutions describe the dynamic picture of a multi-level atom in multi-mode radiation fields. Appendix C presents the application of the formulation in quantum dynamic of magneto-optical trap.

2.5.1 Two-photon transition

Fundamentally a transition frequency from a ground-state to a Rydberg state of an alkali atom is in an order of hundreds THz. There is no available laser having corresponding wavelength to do single-photon excitation. Hence in many Rydberg experiments the two-photon excitation is used. Dynamic of two-photon transition can be studied through a three-level system interacting with two laser fields. In Rydberg case, the system forms a ladder in which successive energies lie higher than the predecessor. The laser field coupling the ground state to the intermediate state is called *probe beam* and the other field, called *coupling beam* couples the intermediate state and the Rydberg state.

2.6 Light-assisted cold collision in blue-detuning regime

This section presents the general concept of light-assisted collision in blue detuning scheme. Landau-Zener formula used in calculation probability of inelastic collision and the physics of two-photon transition.

2.6.1 Landau-Zener model

This section presents semiclassical picture used for describing cold collision in light field. The The Landau-Zener probability that the collision partner remain on the ground

state as it passes once through the interaction region is,

$$P_g = \exp\left(-\frac{\pi\hbar\Omega^2}{2\alpha|p|/\mu}\right) \tag{2.72}$$

where Ω is the Rabi frequency and α is the slope of the difference potential $U(R) = U_e(R) - U_g(R)$ evaluated at the Condon point R_c,

$$\alpha = \left|\frac{d\Delta}{dR}\right|_{R_c} = \left.\frac{dU(R)}{dR}\right|_{R_c} \tag{2.73}$$

The parameter μ is the reduced mass of collision partner. The momentum p is given by the relation to kinetic energy at a particular temperature T.

$$E_{kin} = \frac{p^2}{2\mu} \equiv k_B T \tag{2.74}$$

The probability of exiting the collision on the excited state asymptote after traversing the crossing region twice is

$$P_e^{\infty} = P_g(1 - P_g) \tag{2.75}$$

CHAPTER 3

Rydberg State Revisited for Deterministic Single-atom Source

This chapter presents our proposed mechanism for loading single rubidium atom in an optical dipole trap. The chapter begins, in section 3.1, with an illustrative picture of process for preparing trapped single atom by exploiting the long-range interaction of a Rydberg atom and a ground-state atom. It gives a qualitative understanding how the mechanism strongly induces one-body collisional loss that plays an important role in the single-atom loading achievement. Section 3.2 details the development of experimental conditions that the mechanism comes into operation. These conditions are needed for designing a single-atom trap experiment. In section 3.3, the model of light-assisted collision via two-photon excitation was used to evaluate the possibility in using a molecular Rydberg state of Rb_2 to load single rubidium atom in an optical dipole trap.

3.1 Single-atom loading via light-assisted Rydberg-ground collision

The mechanism for loading single atom is shown in Figure 3.1 and described as following. Suppose an atom is a three-level system; ground state, intermediate state, and Rydberg state. Let atoms be initially loaded into a far-off-resonance optical dipole trap. The interaction between a Rydberg atom and a ground-state atom is represented by a long-range adiabatic potential energy curves that includes both metastable molecule states and repulsive potential. The application of two-photon transition consisting of 780nm and 480nm photons, of which combined frequency is slightly higher than the resonance frequency between the ground state and preselected Rydberg state (measured on asymptotic lines in non-interaction regime), would give raise to the induced collision between ground and Rydberg atoms through the repulsive potential curve. The Condon point R_c is defined as the internuclear distance where the two-photon transition is on a resonance. Since the Rydberg atom only senses weakly repulsive dipole force [42] and

the ground-state atom is tightly pined by the trap, the Rydberg atom tends to slowly drift out from the trap region. Due to its long lifetime, the whole process of collision has completed before the spontaneous emission and hence the *one-body collisional loss* is significantly boosted. As time passes, such collisional loss events continue until there is only one atom left in the trap; hence the determinism of loading a single atom.

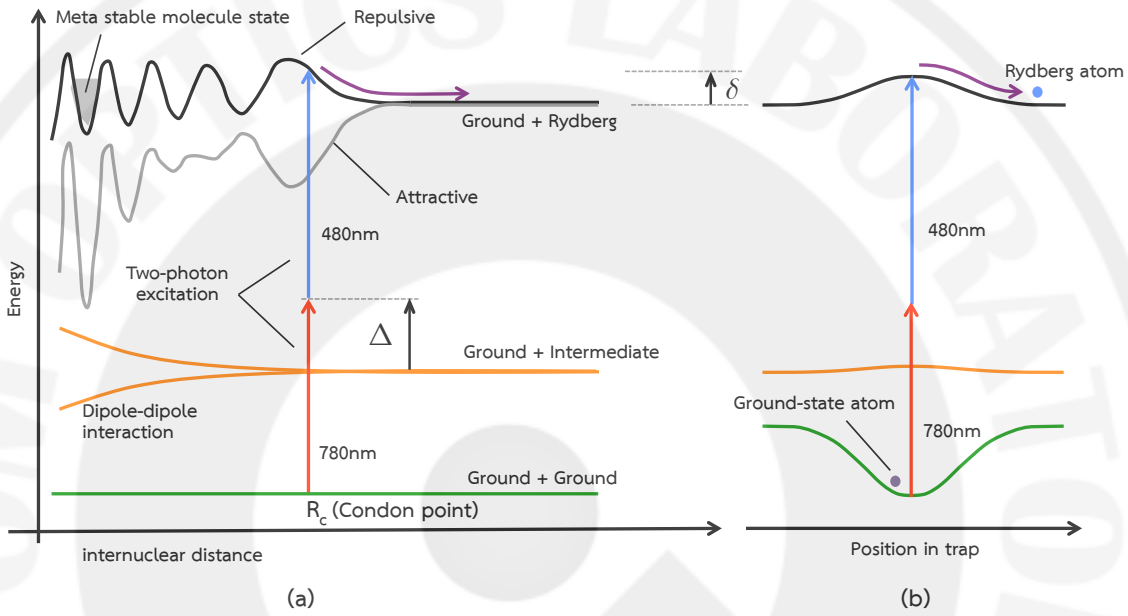

Figure 3.1: a) Potential energy curves of Rydberg-ground interaction and intermediate-ground interaction as function of internuclear distance (orange and black-gray curves respectively). The frequency of 780nm light is far blue-detuned from the intermediate transition by Δ to prevent real excitation to the intermediate state in which the two-photon excitation is influenced. The intermediate-ground state and Rydberg-ground state are coupled by 480nm light. The small blue detuning δ of total frequency is selected such that the excitation takes place whenever two colliding atoms come close at R_c distance. b) Energy level of an atom in optical dipole trap. Considering an atom of a colliding atomic pair excited to the Rydberg state (blue circle), it is not confined by the dipole force any longer and goes away. Hence the other atom (purple circle) remains. Many cycles of this one-body collisional lost process will end at the situation there is only one atom left.

3.2 Loading constraints

Before going further to the practical detail of a single-atom trap experiment, there are two parameters needed to be introduced. First, a parameter called *escape distance* D_{es} is defined as the minimum distance for a particular trap potential that a Rydberg atom with

total energy E needs to move from the center of trap to the point where after decaying to the ground state the residual kinetic energy is still high enough for exiting the trap. This distance can be calculated from

$$D_{es} = w_o \sqrt{\ln\left(\sqrt{\frac{2U_o}{m v_{mp}^2}}\right)}, \tag{3.1}$$

where U_o and w_o are trap depth and $1/e$ radius of trap potential. v_{mp} is the most probable velocity given by Maxwell-Boltzmann statistics and it depends on temperature of atomic ensemble. Second, it is called *drift distance* D_f and defined as the maximum distance that a free Rydberg atom with lifetime τ_o in an atomic ensemble having temperature of T can move from a point to an another point. The analytic expression of this distance is

$$D_f = \sqrt{\frac{2k_B T}{m}} \tau_o, \tag{3.2}$$

where m is the rest mass of an atom. In order to reach the situation where the light assisted one-body collisional loss dominates over any loss processes, the drift distance must be longer than the escape distance,

$$D_f > D_{es}. \tag{3.3}$$

This condition ensures that when a ground-state atom is excited to the Rydberg state the atom will escape the trap after it decays to the ground state.

From the practical point of view, the strength of repulsive interaction between Rydberg atom and ground-state atom fundamentally decreases as principle quantum number n increase. This relation limits the range of available blue detuning δ that can be selected to determine a Condon point R_c. Moreover, smaller δ means the total frequency of excitation fields is closer to single atom resonance. Hence the probability of one-body loss induced by one-body excitation, instead of by induced collision, is higher. This causes a major problem when there is only one atom left in the trap in the presence of excitation laser field. The atom has a chance to be excited to Rydberg state and then drifts out from

the trap, hence single-atom loading efficiency will strongly decrease. Hence there are two crucial conditions that must be satisfied in order to prevent such problem. First, the principle quantum number n must be small in the way that corresponding barrier potential is strong enough in which the detuning δ can be chosen significantly larger than the one-body scattering rate of two-photon transition. Second, to satisfy Eq.(3.3), the trap dimension, w_o, must be smaller than the drift distance determined by the lifetime of the Rydberg state of interest. However, the latter condition is automatically satisfied in a standard 3D optical lattice experiment since the dimension of single lattice site is in order of sub-micron while typical values of drift distance of cold Rydberg atom, having principle quantum number between 30 to 50, lie between 1 μm to few tens μm.

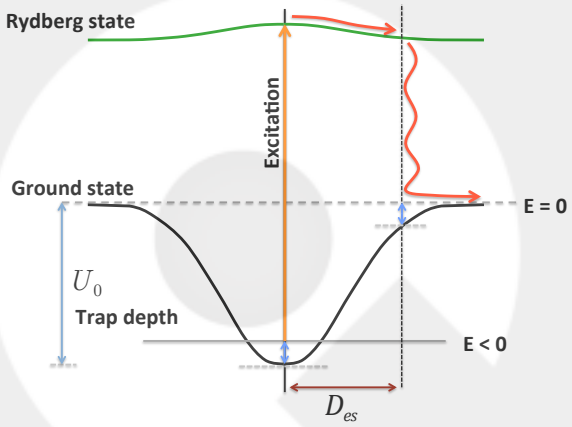

Figure 3.2: Escape distance D_{es} is the minimum distance that the Rydberg atom needs to move for escaping the trap.

In addition to the two presented condition, the density is an important factor needed to be concerned. If the Condon point R_c is larger than averaged separation distance between two adjacent atoms in the trap, at a particular high density, it has a chance that a colliding pair will be excited to a metastable bound state (shaded area in Fig.(3.1)) and then the whole process gets out of control. To fix this problem, the frequency of 480nm light must be precisely tuned to a preselected Rydberg state, of which interaction with a ground state atom has the same Condon point. Therefore an additional required condition is that the density of atomic ensemble must be prepared in which the average separation distance between atoms is larger than the selected Condon point.

3.3 Analysis of single-atom loading probability

The possibility of single-atom loading is evaluated through the probability of occurrence of one-body collisional loss compared to other processes including elastic collision, no collision, two-body collisional loss, and one-body loss via one-body excitation. In principle, to fully characterize the dynamic of cold collision between atoms in light field, one need to treat the problem quantum mechanically using the scattering theory. To simplify the problem, we treat the motion of two colliding atoms in an optical potential classically but excitation semi-classically using the Landau-Zener model presented in Chapter 2. Let define five possible scattering processes relevant in the determination of single-atom loading efficiency as follow:

1. *One-body collisional loss*: collision takes place and one of two colliding atoms escapes the trap after collision finished. If this scattering process dominate, higher probability of loading single atom. This channel is denoted by $D(2|1)$.

2. *Two-body collisional loss*: collision takes place and both of two colliding atoms escape the trap after collision finished. This scattering process reduces the efficiency of single-atom loading. This channel is denoted by $D(2|2)$.

3. *Elastic collision*: collision takes place and both of two colliding atoms still are in the trap after collision because the kinetic energy of each atom dose not change. This channel is denoted by $D(2|0)$.

4. *No collision*: collision does not take place, denoted by $D(2|N)$.

5. *One-body loss via one-body excitation*: an atom can gain additional kinetic energy by scattering with near or on resonance photons. This process heats atomic ensemble and cause trap loss, hence it reduces efficiency of single-atom loading. This process is denoted by $D(1|1)$.

Clearly that the process $D(2|1)$ needs to strongly dominate over the other processes especially $D(2|2)$ and $D(1|1)$ in order to achieve the determinism of single-atom loading.

To look for a possibility under practical conditions, let consider the light-assisted collision between a rubidium Rydberg atom in $35D_{5/2}$ and a ground-state rubidium atom in $5S_{1/2}$ in an optical dipole trap with 10MHz trap depth. Assuming atomic ensemble in the trap is in thermal equilibrium and has temperature of 65 μK. The approximated repulsive adiabatic interaction potential of $5S_{1/2} + 35D_{5/2}$ is shown in Fig.(3.3). This potential was calculated by using e-B scattering length presented in Chapter 2. The state $5P_{3/2}$ is the intermediate level in this case. Throughout the discussion, the condition Eq.(3.3) is assumed to be satisfied since it can be achieved in typical dipole trap experiment without special effort.

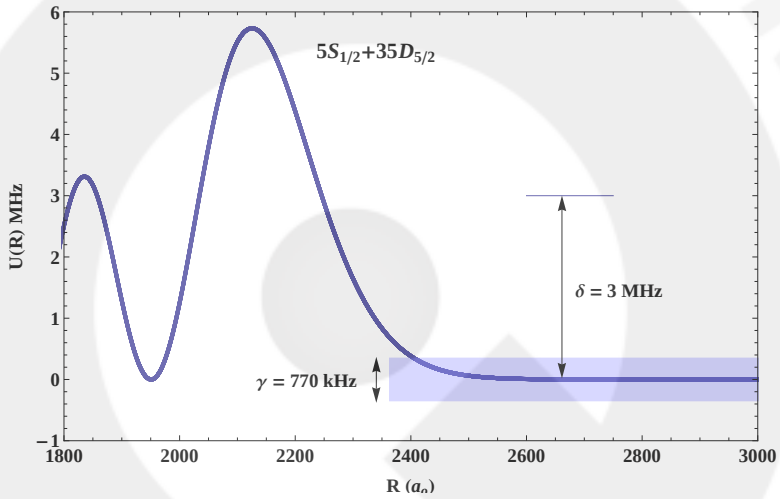

Figure 3.3: Approximated repulsive semi-molecular potential of $5S_{1/2} + 35D_{5/2}$.

One-body excitations of both $5P_{3/2}$ and $35D_{5/2}$ contribute to the occurrence of $D(1|1)$ process. At first glance minimizing the occurrence of $D(1|1)$ caused by excitation of $5P_{3/2}$ can be done by setting far detune Δ from D2 line resonance. However, Eq.() implies that if Δ is too large, the two-photon excitation rate will be significantly reduced, hence occurrence of $D(2|1)$. To find an optimum range of Δ, it is set to be an independent variable that all possible occurrences are plotted as function depending on it. For the contribution from one-body excitation of $35D_{5/2}$, the two-photon detuning δ is thus chosen to be 3 MHz above asymptotic line as shown in Fig.(3.3). This is a reasonable value because the power broadening of two-photon transition of isolated atom is only around 770 kHz, hence low one-body loss via one-body excitation can be expected. In addition, the

detuning δ of 3 MHz is less than the trap depth and hence excitation at the Condon point does not induce two-body collisional loss and also whenever a colliding pair is excited to the repulsive region, one can ensure $D(2|1)$ process is forced to take place.

The source of $D(2|2)$ arises from the light-assisted collision between an atom in $5S_{1/2}$ and its colliding pair in $5P_{3/2}$ state. The collision can be induced by 780 nm light whose detuning Δ is blued from resonance, in this case it is 100 MHz. The dipole-dipole interaction of $5S_{1/2} + 5P_{3/2}$ can cause energy shift in which the frequency of detuned 780 nm becomes on resonance of semi-molecular potential. Since the detuning of 100 MHz is much larger than the trap depth, this type of collision causes $D(2|2)$. However both $D(2|1)$ and $D(2|2)$ take place at different Condon points, R_{C1} and R_{C2} respectively. Since R_{C1} is normally longer than R_{C2}, the occurrence of $D(2|2)$ can be strongly suppressed by preparing the atomic ensemble in a low density. Fig.(3.4) shows the probability distribution function of separation distance of the two adjacent atoms at density of 3×10^{11} cm^{-3}. The proportion of a colliding pair having the separation distance in which the light-assisted collision of $5S_{1/2}$ + $35D_{5/2}$ takes place is higher than the proportion of $5S_{1/2}$+$5P_{3/2}$. Therefore $D(2|1)$ collision through $5S_{1/2}$+$35D_{5/2}$ interaction dominates over $D(2|2)$.

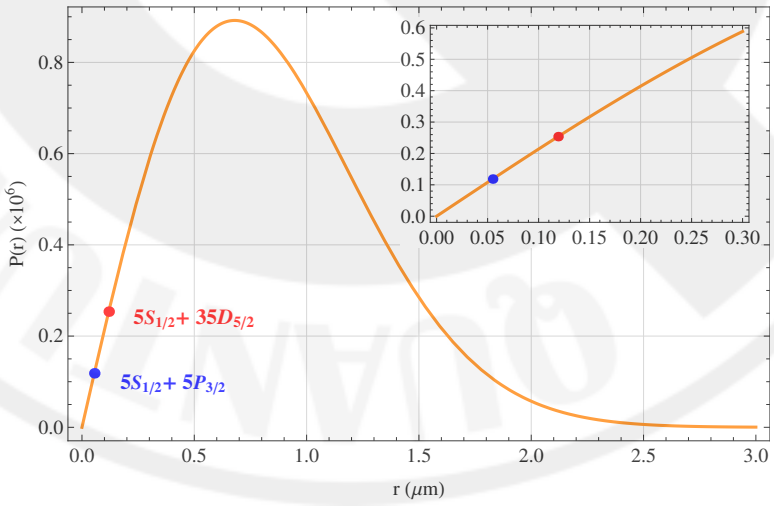

Figure 3.4: Distribution of inter-particle distance

Fig.(3.5) shows the approximated strength in arbitrary unit of occurrences of each scattering process as function of intermediate detuning Δ. This plot was obtained from

applying Landau-Zener model and taking into account that $D(2|1)$ and $D(2|2)$ occur at different Condon points. At detuning of 100 MHz, the occurrence of $D(2|1)$ dominates over $D(2|0)$, $D(1|1)$, and $D(2|2)$. $D(2|N)$ process has the maximum strength but fundamentally it does not affect the efficiency of single-atom loading except the time used to switch on excitation lasers.

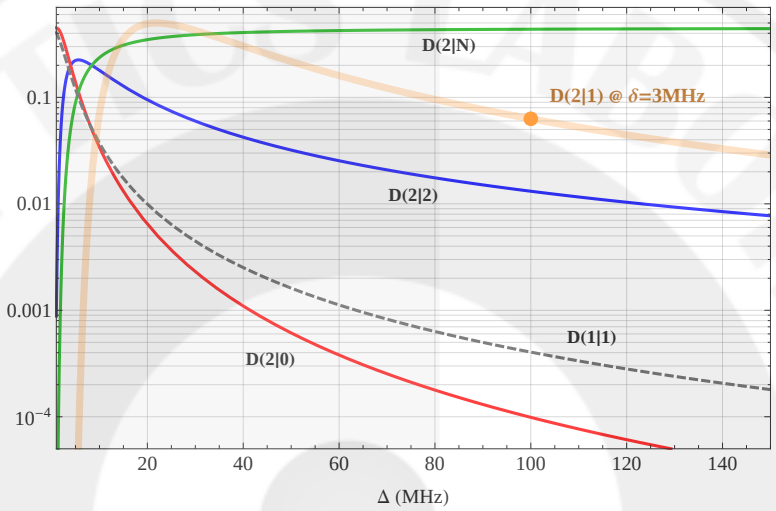

Figure 3.5: Occurrence strength of scattering processes as function of intermediate detuning. The gray shaded area covers the range of the detuning from 0 MHz to 80 MHz in order to indicate the safe range from one-body excitation that induces $D(1|1)$.

3.4 Summary

Apart from all crucial conditions presented in this chapter, there however are advantages of our proposed mechanism over the process implemented in [17]. First, it does not need the large blue detuning, that may induces two-body collisional loss event. Hence the high probability of one-body collisional loss can be expected. Second, although the fine-tuning on the two-photon excitation is needed, the overall performance does not strongly depend on trap depth and all uncontrollable thermal parameters, e.g. energy shared between collision pair, do not determine the one-body loss event or single-atom loading efficiency. Therefore this mechanism can be applied to the preparation of optical lattices where each well is filled with just single atom.

CHAPTER 4

Investigation of Repulsive Molecular Rydberg State

This chapter reports the experimental investigation and exploration of the adiabatic repulsive potential curve of Rb_2 in Rydberg state and the possibility of exploiting such interaction for the sake of single-atom loading technique. Section 4.1 describes the optical circuits designed for preparing the optical frequencies required for the Rydberg excitation and detection of rubidium-87. In this experiment atoms are initially cooled and trapped by the magneto-optical trap and then loaded into one-dimensional optical lattice before applying Rydberg excitation. Section 4.2 presents the diagnostic of atomic ensemble in the lattice. The strategy for investigation of repulsive interaction of Rb_2 and the experimental results are presented in section 4.3.

4.1 Experimental setup

The section details the optical setup of laser system required for operating the magneto-optical trap, one-dimensional optical lattice, and two-photon excitation of Rydberg states of rubidium-87 atom.

4.1.1 Magneto-optical trap lasers

Generation of a rubidium magneto-optical trap (MOT) requires two optical frequencies: MOT-cooling laser and MOT-repumping laser. The frequencies of these laser differ by 6.8GHz in rubidium-87. The optical schematics of cooling and repumping lasers are shown in Fig.(4.1) and Fig.(4.2) respectively. The cooling laser serves the optical frequencies for both MOT loading and MOT imaging processes. The whole laser system is based on phase lock technique using two the external cavity diode lasers (ECDL) with Littrow configuration. The output frequency of ECDL 0 is stabilized using standard saturated absorption spectroscopy and used as the reference frequency in phase locking. The frequency is locked with respect to the crossover peak $F = \mathrm{CO}(1,3)$ D2 line. ECDL 1

serves the main power of cooling laser using the tapered amplifier (TA). The output frequency of ECDL1 is stabilized with frequency of ECDL0 using the phase locking. The repumping laser is obtained from ECDL2 whose output frequency is locked at transition frequency $F = 1 \rightarrow F' = 2$.

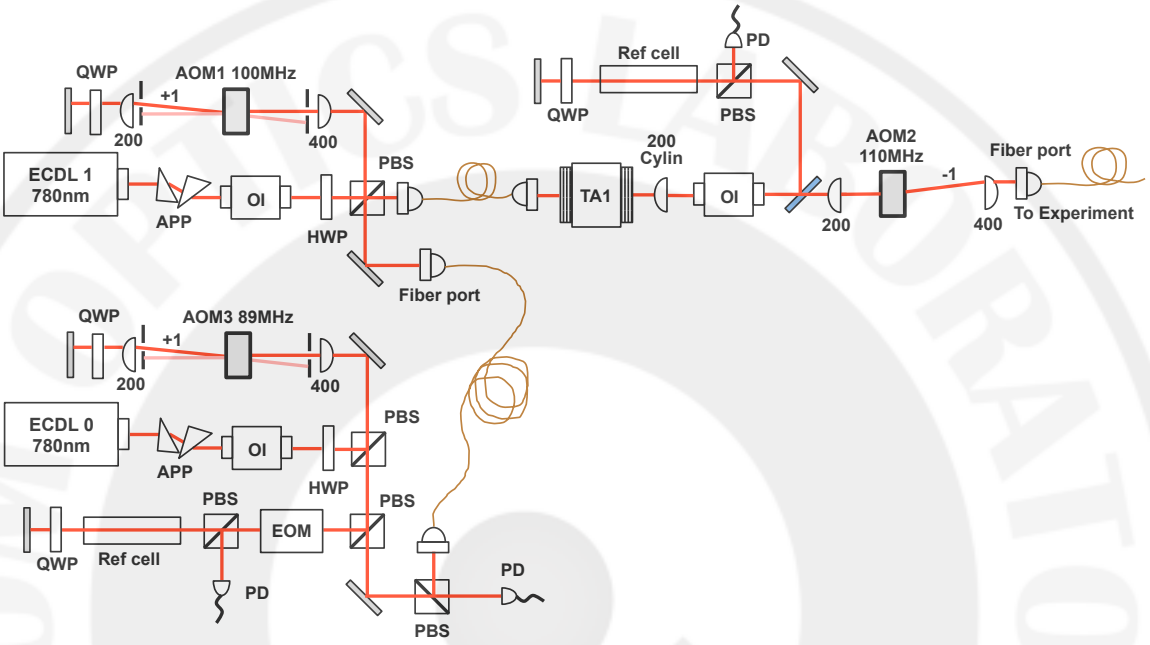

Figure 4.1: Optical schematic of MOT cooling laser. The phase locking technique is used to stabilize output frequency of ECDL1 with respect to ECDL0. The output power was amplified by the tapered amplifier. OI = optical isolator, HWP = haft-wave plate, QWP = quarter-wave plate, APP = anamorphic prism pair, PBS = polarizing beam splitter

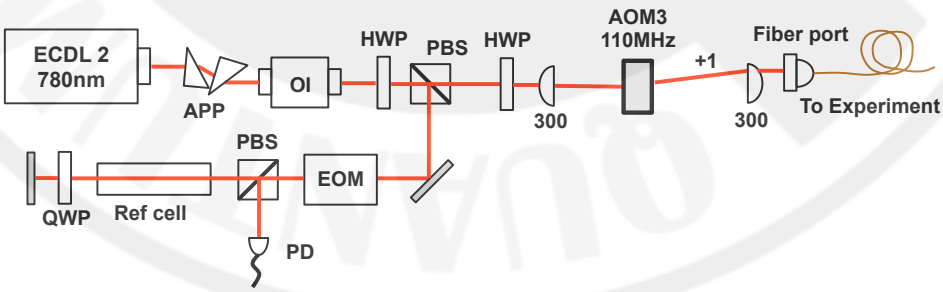

Figure 4.2: Optical schematic of MOT repumping laser.

4.1.2 Optical lattice laser

The lattice trap laser produces a laser beam for generating an one-dimensional optical lattice formed by the cavity in the chamber. In this experiment, the lattice laser is a homemade external cavity diode laser (ECDL3) operating at the wavelength of 808 nm. The laser was controlled via a homemade current controller and a homemade temperature controller. The dipole laser has a total optical output power of 100mW but due to the non-Gaussian profile the power much loss by coupling into a fiber. Hence the final power before going into the experiment is 9 mW. The frequency of laser was stabilized to a mode of tranfercavity using Pound-Drever-Hall technique. The schematic of optical setup around the lattice laser is shown in Fig.(4.3).

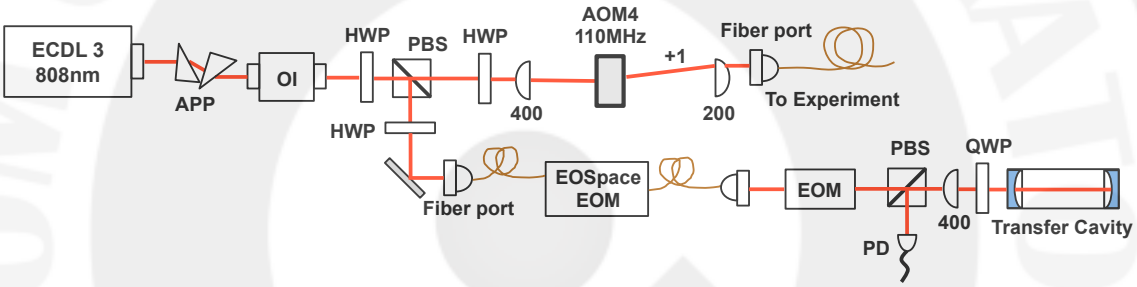

Figure 4.3: Optical schematic of optical lattice laser.

4.1.3 Probe laser

The optical schematic of probing lasers is shown in Fig.(4.4). The optical frequency used for the Rydberg excitation was derived from the external cavity diode lasers (ECDL 4) based on the Littrow configuration. ECDL 4 is a homemade laser system using an anti-reflection coated (AR) laser diode as a light source in order to avoid mode hopping. The output frequency is stabilized with the transfer cavity via a standard Pound-Drever-Hall configuration. In order to set the stabilized frequency with respect to transition frequency of rubidium-87. The computer controller AOM5 and EOSpace EOM were used to adjust the locked frequency according the the error signal obtained from the saturated absorption spectroscopy.

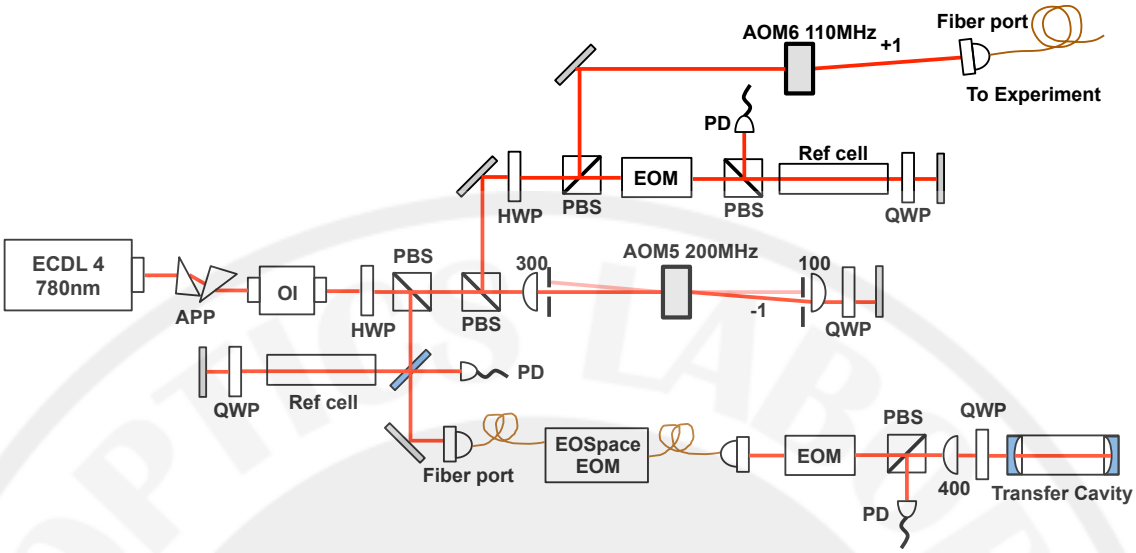

Figure 4.4: Optical schematic of probe laser for Rydberg excitation.

4.1.4 Coupling laser

Fig.(4.4) depicts the optical schematic of 480 nm laser. The laser serves the optical frequency used for two-photon transition of Rydberg state as the coupling laser. Since there is no available laser diode directly emits 480 nm light, a system of doubling frequency was exploited. The 960 nm laser (ECDL5) was used to produce 480nm light by coupling the 960nm light into the Bow-tie cavity containing the crystal used for produce doubled frequency photons. Due to low efficiency of doubling frequency creation. The tapered amplifier (TA2) was used to increase the overall output power of 480nm coupling light. The seed frequency of 960nm laser is stabilized with the transfer cavity using a standard Pound-Drever-Hall configuration. The frequency of coupling light is tuned can controller by computer-controlled EOSpace EOM.

4.1.5 Experimental geometry

Fig. (4.6) shows the experimental configuration used for study trap loss due to light-assisted cold collision between Rydberg atom and ground state atom. The one-dimensional optical lattice is formed by linear polarized 808nm wavelength light in high finesses cavity. The power of 808nm laser is 9 mW before going into the cavity and

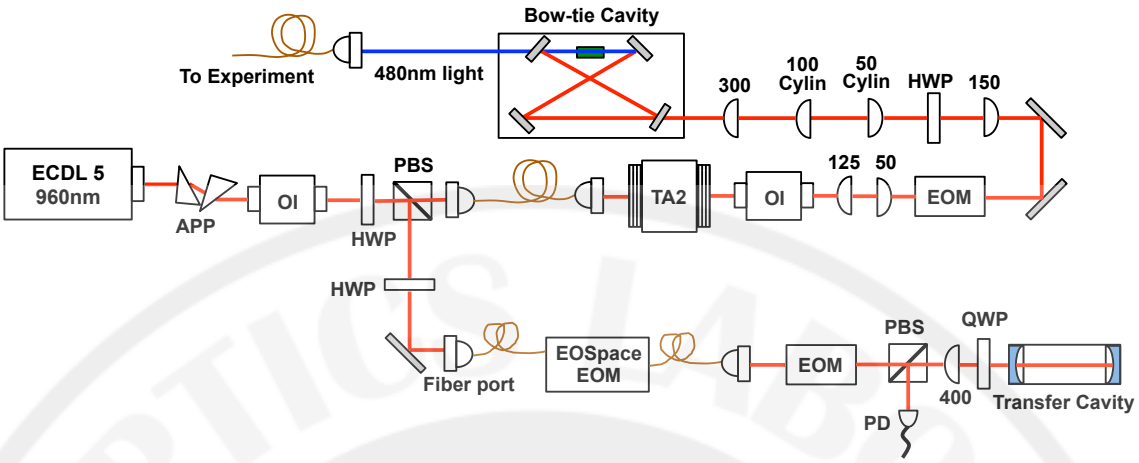

Figure 4.5: Optical schematic of coupling laser for Rydberg excitation.

this leads to the trap depth (total AC Stark Shift of $5^2S_{1/2}F = 1, 2$) of 7 MHz or 380 μK. The magnetic field of 6.5 G for defining a quantization axis is generated by a pair of Helmholtz coil. The field direction is downward, hence defines $+z$ axis direction. To measure trap loss, we perform atom number counting by absorption imaging method. The 780nm imaging beam is directed from the bottom pass through the lattice and then go to the camera. The imaging beam has σ^- polarization with respect to direction of magnetic field. In the same direction, there is a 780nm probe beam for applying two-photon transition. The 480nm coupling beam goes into the chamber in the same direction as 808nm dipole trap beam. This helps the coupling beam to interact with almost atoms in the lattice. Note that the linear polarization of the coupling beam is superposition of σ^+ and σ^- along the quantization axis. The MOT-repumping beam is setup to pass the lattice along y axis. Fig. (4.7) shows some parameters about the experiment.

4.2 One-dimensional optical lattice diagnosis

Since the nature of light assisted collision depends on many factors including average separation distance between two adjacent atoms, motional temperature of sample and the rate of excitation to a semi-molecular potential, the efficiency of single-atom loading also depends on such factors. Hence the atomic sample needs to be characterized in order to get necessary information needed for exploring the repulsive interaction between

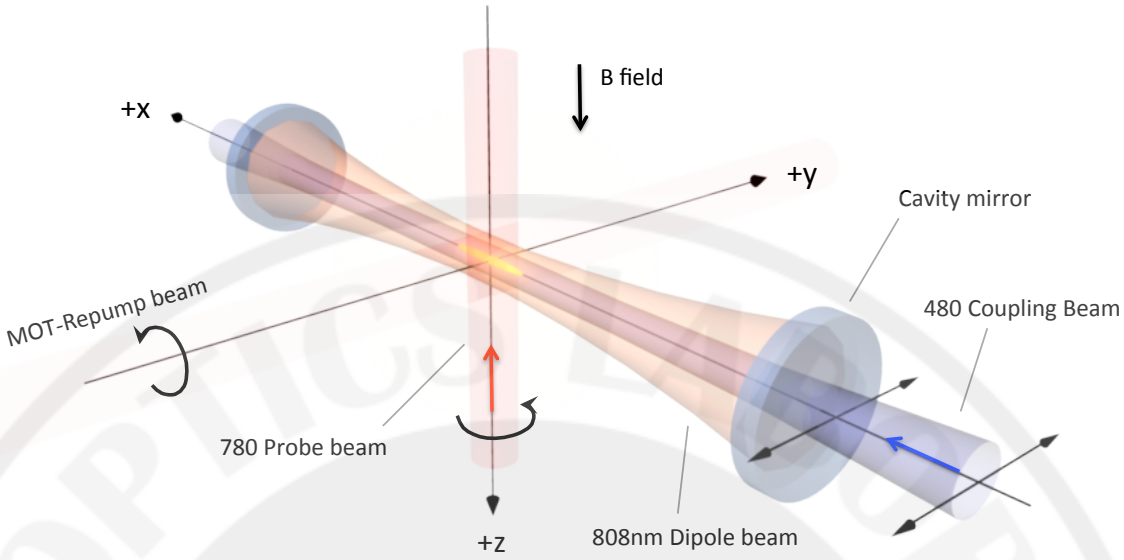

Figure 4.6: The configuration of laser beams used in the experiment: The red and blue arrows show propagation direction of 780nm probe beam and 480nm coupling beam respectively. The two double arrows on the right hand side represent linear polarization direction of 808nm dipole beam and the coupling beam respectively. MOT-repump beam propagates in $+y$ direction with circular polatization. The downward magnetic field B define quantization axis $+z$.

a Rydberg atom and a ground-state atom. The characteristics of atomic ensemble in the optical lattice including number of stored atoms, trap lifetime, density distribution, and temperature are presented in this section.

4.2.1 Trap lifetime of optical lattice

Under the vacuum condition operated in this work and in the absence of any laser light except the dipole laser, loss of trapped atoms in the optical lattice can occur by collision with thermal gases in the chamber. The rate of such collision determines the lifetime of atoms in the trap. Fig.(4.8) shows the measured number of stored atom decaying exponentially as function of time. Due to temperature fluctuation caused by the heated rubidium getter, the typical values of trap lifetime achieved in the experiment is limited to 580 ms.

Experimental Parameters

- MOT Beam Power (each) 30 mW
- Cavity Specification
  - Length 6.3 cm
  - Radius of curvature of cavity mirrors 10 cm
  - Diameter of cavity mirros 1.27 cm
  - Waist at 808 nm 109 μm
  - Rayleigh range 808 nm 4.6 cm
  - Finsees at 808 nm 3000
- 480nm Power (into chamber) 70 mW
- 480nm Waist (at clound) 40 μm
- 808nm Power (into chamber) 9 mW
- Magnetic field (quantization) downward
- Magnification (Imaging) 2.23
- 780 Probe Power 0.81 μW
- 780 Probe Waist 530 μm
- 780 Probe detuning form ($5^2P_{3/2}$) +100 MHz

Figure 4.7: Experimental parameters in Rydberg experiment

4.2.2 Temperature of optical lattice

Considering the thermal cloud of lattice and assuming that trapped atoms are in a thermal equilibrium where the Maxwell-Boltzmann static is valid, the temperature of cold atomic cloud can be determined from the free-space ballistic thermal expansion. The measurement begins by switching off the lattice beam. After a delay time τ, the camera shutter is opened and the probe beam is switched on and then an absorption image of atomic cloud is captured. Due to the cloud is distributed in a Gaussian profile, the standard deviation σ of the distribution can be extracted from the image. By varying the delay time and collecting the corresponding $\sigma(\tau)$, the temperature T can be calculated by apply a linear fitting to the equation [43]

$$\sigma^2(\tau) = \sigma_o^2 + \frac{k_B T}{m}\tau^2, \tag{4.1}$$

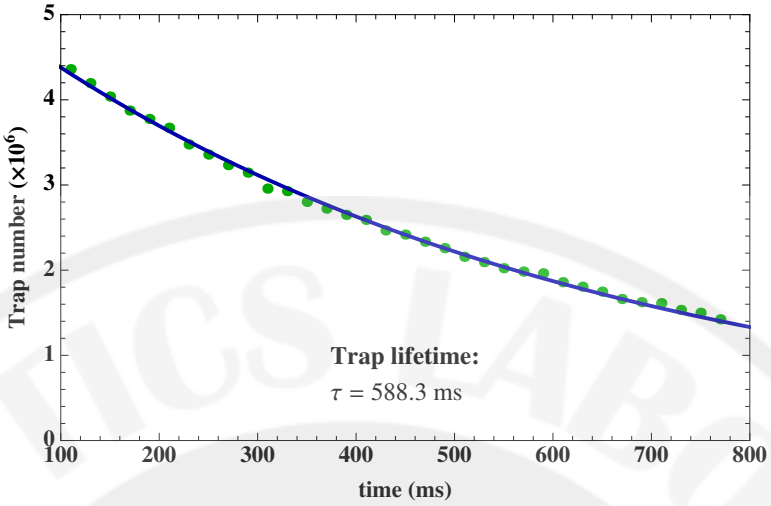

Figure 4.8: Measured trap lifetime of rubidium atoms in the optical lattice. Trap lifetime of 588.3 ms was obtained by fitting the data with exponential decay function.

where m is the mass of a rubidium atom in SI unit. The plot of squared standard deviation versus squared delay time is shown in Fig.(4.9) and the fit corresponds to a temperature of 65 μK. However the temperature gradually increases over time due to heating processes contributed by interaction with 808nm lattice laser.

4.2.3 Density distribution of optical lattice

According to the Maxwell-Boltzmann statistic, trapped atoms stored in an optical potential $U(\vec{\boldsymbol{r}})$ at equilibrium temperature T have density distribution $n(\vec{\boldsymbol{r}})$ given by

$$n(\vec{\boldsymbol{r}}) = n_o \exp\left(-\frac{U(\vec{\boldsymbol{r}})}{k_B T}\right), \tag{4.2}$$

where n_o is the peak density and $\vec{\boldsymbol{r}}$ is position vector. Trap potential of optical lattice can be approximated as the 3D harmonic potential that has cylindrical symmetry. Consequently, the density distribution of atomic cloud has Gaussian profile. Gaussian fit of the distribution along axial and radial directions are shown in Fig.(4.10). It should be noted that the distribution shown in the figure was obtained after letting atomic cloud ballistically expands for 1.5 ms before the images were taken. In order to find the true density distribution profile, the measured temperature and Eq.(4.1) are used to calculate

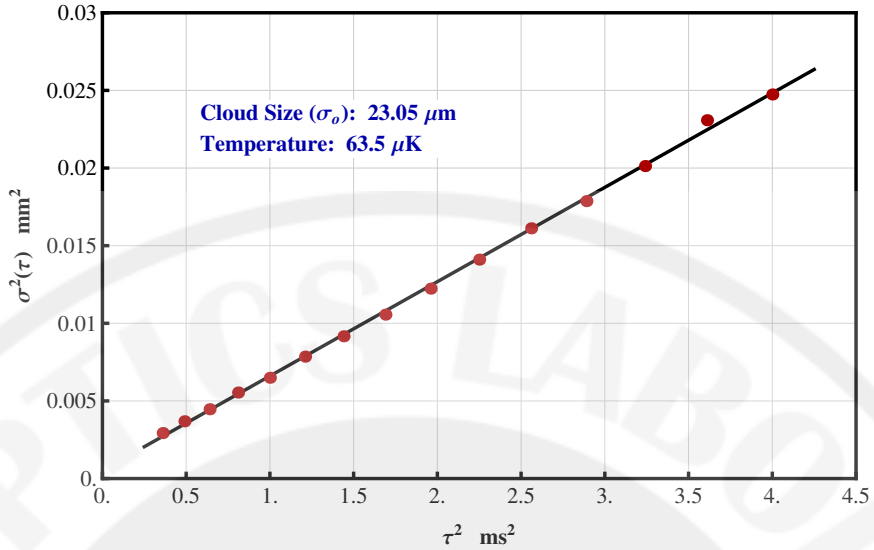

Figure 4.9: Temperature measurement by free-space ballistic expansion method. The data (red points) are fitted with Eq.(4.1).

initial standard deviation of Gaussian profile before releasing the trap. The distribution of number of stored atoms in each lattice site is shown in Fig.(4.11).

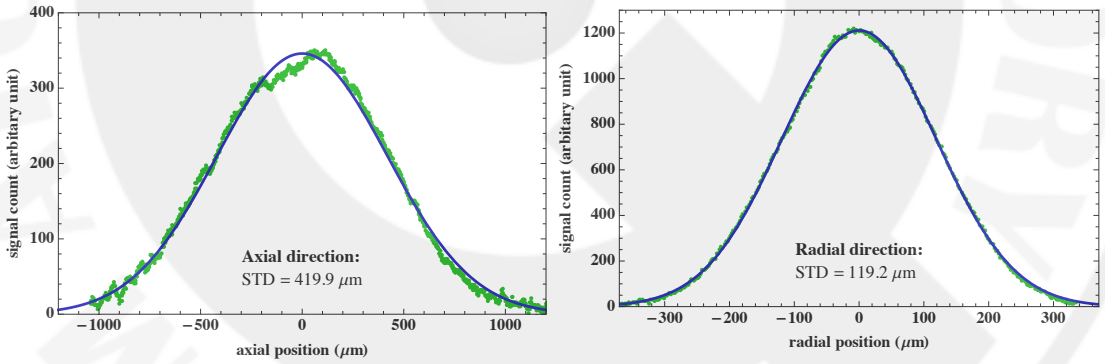

Figure 4.10: Gaussian fitted profile represents how position of trapped atoms are distributed in the trap. The signal count data were obtained from converting the absorption image of atomic cloud Fig.(4.18)(right).

In a single lattice site, the standard deviation of atomic cloud distribution along the axial direction is much smaller than the typical range of interaction between a Rydberg atom and a ground-state atom. The density distribution appropriated for this work is represented in 2D.

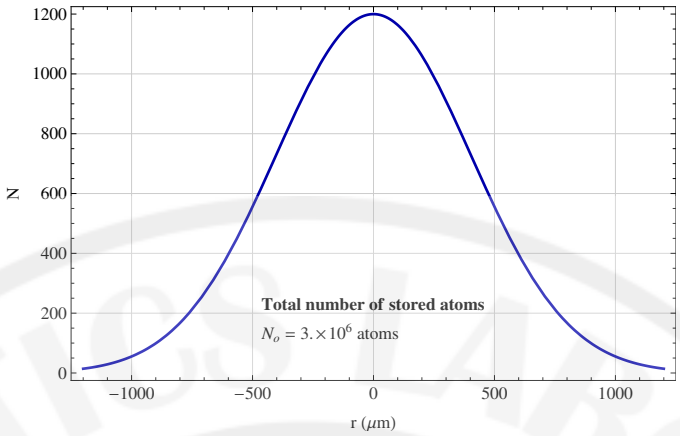

Figure 4.11: The distribution of number of trapped atom along cavity axis.

4.3 Trap loss due to blue-detuned two-photon excitation

This section details the experimental procedure to investigate and explore the possibility of exploiting a repulsive interaction between a Rydberg rubidium atom and a ground-state atom. In order to confirm the existence of a repulsive Rydberg-ground interaction that has a practical capability of supporting our mechanism, the trap loss measurement due to blue-detuned Rydberg excitation needs to be performed. There are two types of measurement presented in this work.

4.3.1 Trap loss as function of detuning

The first type of this measurement is done by comparing the number of atoms remaining in the trap before and after applying the Rydberg excitation lasers whose optical frequency is varied across the resonance frequency. Basically, the probability of trap loss would be maximum when the optical frequency of excitation light is resonant with Rydberg transition frequency and it decreases when the frequency of the laser is off the resonance.

4.3.2 Trap loss at fixed detuning

The second type of trap loss measurement is performed by fixing the detuning above the one-body excitation resonance. Then the remaining number of stored atom is plotted as function of probing time.

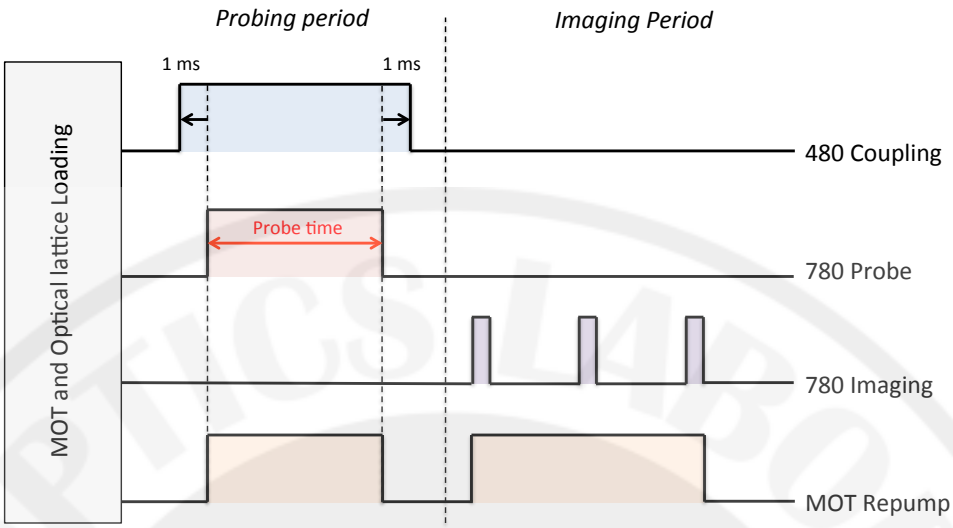

Figure 4.12: Time sequence of experiment: The 480nm coupling beam is turned on 1ms before 780nm probe beam to avoid trap loss due to 780nm light. MOT-repumping beam is also turned on over the probing period. This helps to pump atoms that decays from the Rydberg state to $5^2S_{1/2}F = 1$ go back to $5^2S_{1/2}F = 2$ for next Rydberg excitation.

4.3.3 Time sequence and results

The time sequence of the experiment is shown in Fig. (4.12). The cold atomic ensemble is initially prepared from standard magneto optical trap (MOT) while the optical lattice is turned on. This produces dark magneto optical trap with low temperature. After MOT loading period, the intensity of MOT beams is then decreased and its detuning (from $5^2S_{1/2}F = 2 \rightarrow 5^2P_{3/2}F' = 3$) is gradually changed from -18 MHz to -185 MHz for performing sub-Doppler cooling. The cloud after this cooling process has temperature of 65 μK. In the probing period, the 480nm coupling beam is turned on 1ms before 780nm probe beam for preventing any trap loss due to 780nm light. The detuning and power of the probe beam is fixed at blue-detuning +100 MHz from the intermediate state, $5^2P_{3/2}$ see Fig (4.13), and 0.8 μW respectively. This corresponds with the Rabi rate of 0.8 MHz. The detuning of the 480nm coupling beam is varied from 0 MHz to 20 MHz with respect to the effective bare transition ($5^2S_{1/2} \rightarrow 50^2S_{1/2}$ and no AC Stark Shift). The coupling beam has power of 70 mW and this corresponds with the effective two-photon transition rate of 54 kHz, $\Omega = \Omega_1\Omega_2/(2\Delta)$. The Fig. (4.14-4.17) show the measured number of

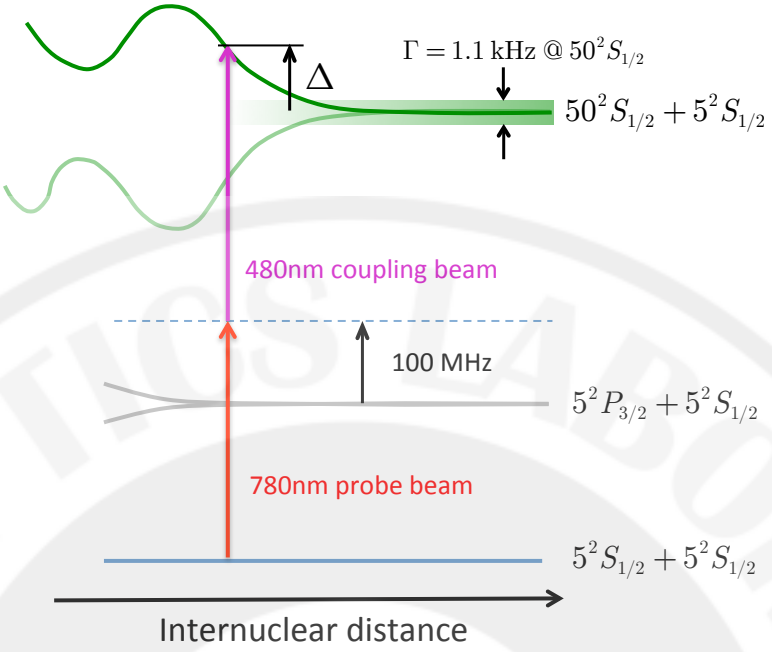

Figure 4.13: Excitation Scheme of Rydberg experiment: the energy levels presented here are bare states, no AC Stark shift.

trapped atom as function of detuning Δ for 100 ms and 20 ms probing time. For imaging period, the 780nm imaging beam is derived from the MOT beam with detuning of -2.2 MHz from $5^2S_{1/2}F = 2 \rightarrow 5^2P_{3/2}F = 3$ transition. The pulse length of imaging beam is 100 μs and the optical lattice is tuned off 1.5 ms before taking images. This trap dropping releases the cloud expanding and hence reduces the optical density of atomic cloud. This improves efficiency of trapped atom counting. There are three images taken in the detection process; with atom, without atom, and background. These images are taken with 35 ms apart from each other. To extract the number of trapped atoms, the background is subtracted from the first two images and then the second image is subtracted from the first image. The trap number is given by integration over the area of atomic cloud. Fig. (4.18) shows an example of atomic cloud image after subtraction.

4.4 Summary and outlook

Up to present, we have performed theoretical analyses, numerical calculations and experiment for investigating whether or not the Rydberg-ground repulsive adiabatic po-

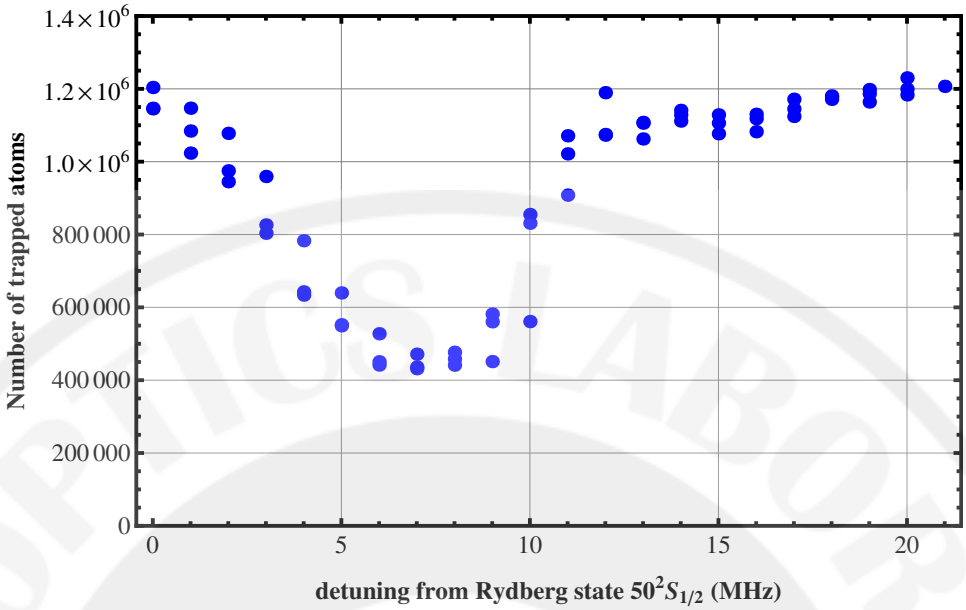

Figure 4.14: Number of remaining trapped atom after 100 ms of probing time as function of detuning Δ from Rydberg state $50^2S_{1/2}$. The lowest dip at 7 MHz shows trap loss due to on-resonance Rydberg excitation compensated with AC Stark shift of ground state $5^2S_{1/2}$. The other small dip at 15 MHz shows trap loss due to blue-detuning excitation.

tential energy have strong enough potential for leading to the deterministic single-atom loading in an optical micro-trap. In the future, we are looking for the scalable single-atom source on demand based on this technique and also the discussion of combination with the collisional blockade.

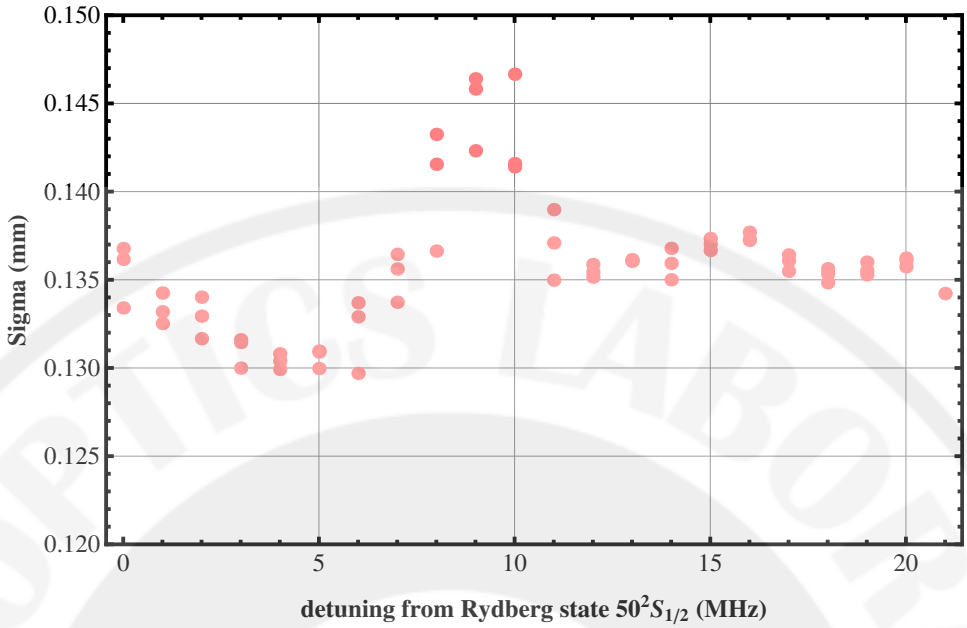

Figure 4.15: This plot shows the standard deviation of atomic cloud Gaussian fitting after 100 ms probing time. At 15 MHz detuning it shows heating (increase in cloud size) due to blue-detuning Rydberg excitation.

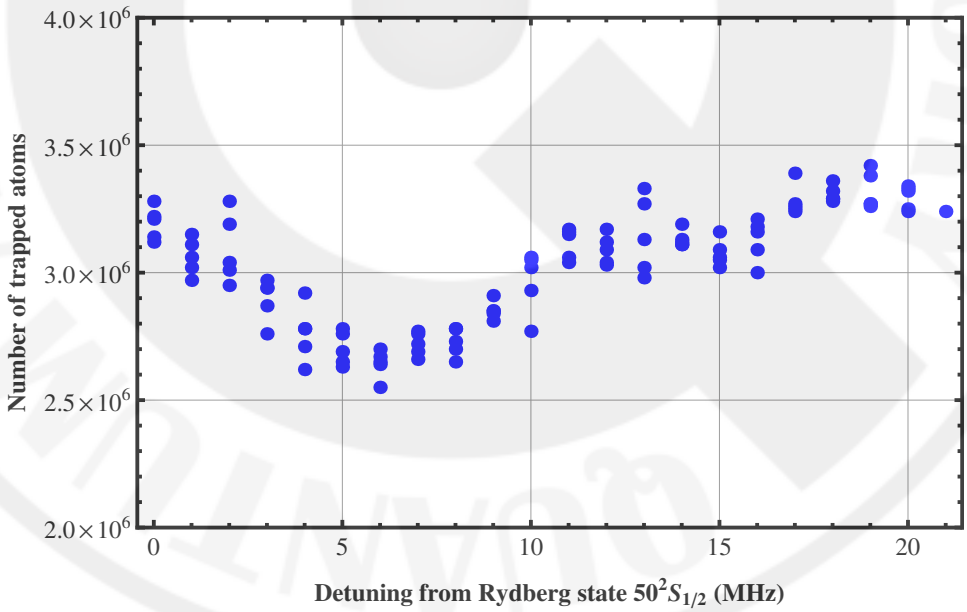

Figure 4.16: Number of remaining trapped atom after 20 ms of probing time as function of detuning Δ from Rydberg state $50^2S_{1/2}$. The lowest dip at about 6 MHz shows trap loss due to on-resonance Rydberg excitation compensated with AC Stark shift of ground state $5^2S_{1/2}$. The next small dip at 15 MHz shows the trap loss due to blue-detuning excitation.

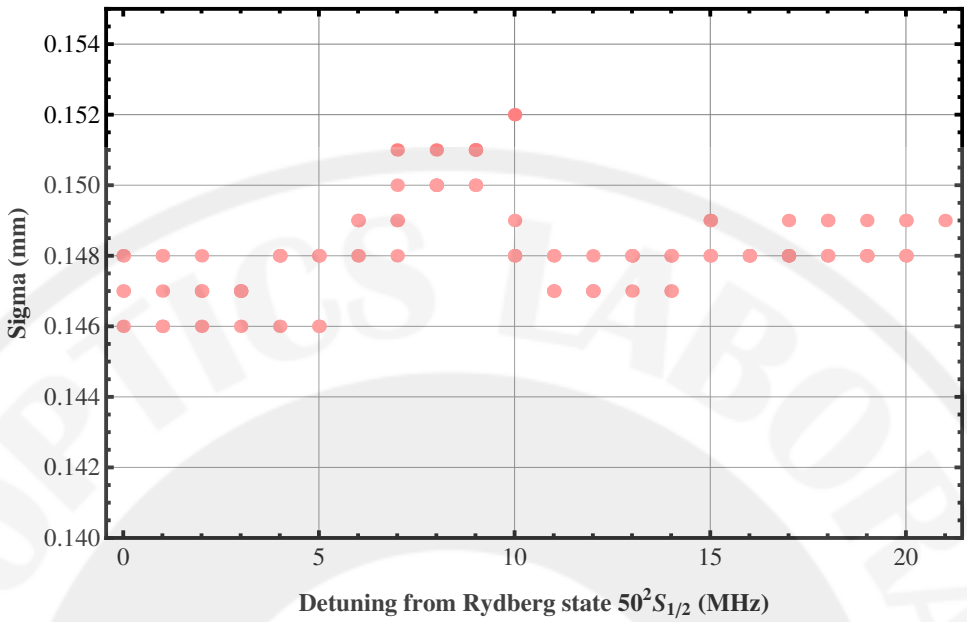

Figure 4.17: This plot shows the standard deviation of atomic cloud Gaussian fitting after 20 ms probing time. At 15 MHz detuning it does not show cleary heating because short excitation time.

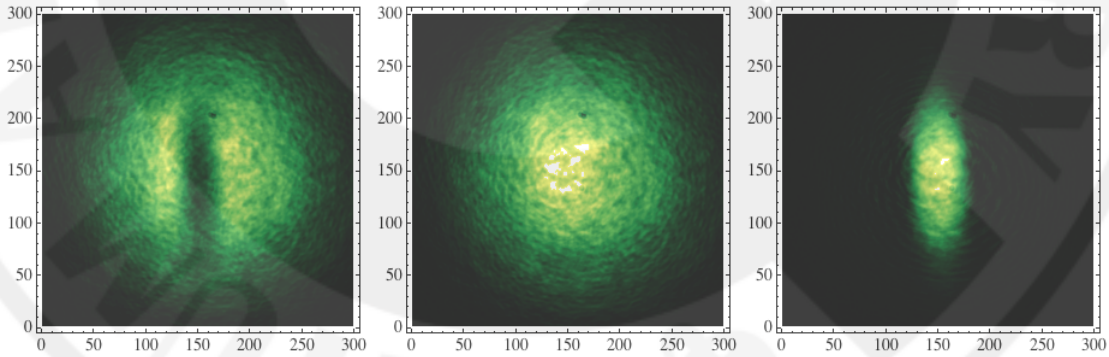

Figure 4.18: In imaging process, the first image (left) is taken while trapped atom are released 1.5ms before taking image and expanding ballistically. The second image (center) is taken after waiting until there is no atoms in the area of imaging. Theses images are subtracted from each other for getting the cloud of atom in the lattice (right). The raw images have resolution of 2048x2048 pixels. Gaussian resmapling method is used to reduce the resolution down to 512x512 pixels. The totoal number of trapped atom is 3 million.

REFERENCES

[1] D. DiVincenzo, "The physical implementation of quantum computation," *Fortschritte der Physik: Progress of Physics*, vol. 48, 2000, p. 771.

[2] D. Deutsch, "Quantum theory, the church-turing principle and the universal quantum computer," *Proc R Soc. London*, vol. A400, 1985, p. 97.

[3] *Advanced Research and Development Activity (ARDA)*. Quantum Information Science and Technology Roadmap, 2004.

[4] D. Wineland and H. Dehmelt, "Proposed $10^4\delta\nu/\nu$ laser fluorescence spectroscopy on Ti^+ mono-ion oscialltor," *Bull. Am. Phys. Soc.*, vol. 20, 1975, p. 637.

[5] T. Hansch and A. Schawlow, "Cooling of gases by laser radiation," *Opt. Commun.*, vol. 13, 1975, p. 68.

[6] D. Wineland and W. Itano, "Laser cooling of atoms," *Phys. Rev. A*, vol. 20, 1979, p. 1521.

[7] S. E. Hamann, D. L. Haycock, G. Klose, P. H. Pax, I. H. Deutsch, and P. S. Jessen, "Resolved-sideband raman cooling to the ground state of an optical lattice," *Phys. Rev. Lett.*, vol. 80, 1997, p. 4149.

[8] W. Demtrober, *Laser Spectroscopy: Basic Concepts and Instrumentation*. Springer, 3rd ed., 2003, p. 150, ISBN: 3-540-65225-6.

[9] I. Bloch, "Ultracold quantum gases in optical lattices," *Nature Physics*, vol. 1, 2005, p. 23.

[10] F. Ruschewitz, D. Bettermann, J. L. Peng, and W. Ertmer, "Statistical investigations on single trapped neutral atoms," *Europhys. Lett.*, vol. 34, 1996, p. 651.

[11] D. Haubrich, H. Schadwinkel, F. Strauch, B. Ueberholz, R. Wynands, and

D. Meschede, “Observation of individual neutral atoms in magnetic and magneto-optical traps,” *Europhys. Lett.*, vol. 34, 1996, p. 663.

[12] J. Ye, D. W. Vernooy, and H. J. Kimble, “Trapping of single atoms in cavity qed,” *Phys. Rev. Lett.*, vol. 83, 1999, p. 4987.

[13] D. Frese, B. Ueberholz, S. Kuhr, W. Alt, D. Schrader, V. Gomer, and D. Meschede, “Single atoms in an optical dipole trap: Towards a deterministic source of cold atoms,” *Phys. Rev. Lett.*, vol. 85, 2000, p. 3777.

[14] S. Nubmann, M. Hijlkema, B. Weber, F. Rohde, G. Rempe, and A. Kuhn, “Submicron positioning of single atoms in a microcavity,” *Phys. Rev. Lett.*, vol. 95, 2005, p. 173602.

[15] W. S. Bakr, J. I. Gillen, A. Peng, S. Folling, and M. Greiner, “A quantum gas microscope for detecting single atoms in a hubbard-regime optical lattice,” *Nature*, vol. 462, 2009, p. 74.

[16] N. Schlosser, G. Reymond, and P. Grangier, “Collisional blockade in microscopic optical dipole traps,” *Phys. Rev. Lett.*, vol. 89, 2002, p. 023005-1.

[17] T. Grunzweig, A. Hilliard, M. McGovern, and M. F. Andersen, “Near-deterministic preparation of a single atom in an optical microtrap,” *Nature Phys.*, vol. 6, 2010, p. 951.

[18] A. V. Carpentier, Y. H. Fung, P. Sompet, A. J. Hilliard, T. G. Walker, and M. F. Andersen, “Preparation of a single atom in an optical microtrap,” *Laser Phys. Lett.*, vol. 10, 2013, p. 125501.

[19] V. Bendkowsky, B. Butscher, J. Nipper, J. P. Shaffer, R. Low, and T. Pfau, “Observation of ultralong-range rydberg molecules,” *Nature*, vol. 453, 2009, p. 1005.

[20] P. Sompet, A. V. Carpentier, Y. H. Fung, M. McGovern, and M. F. Andersen, “Dynamics of two atoms undergoing light-assisted collisions in an optical microtrap,” *Phys. Rev. A*, vol. 88, 2013, p. 051401.

[21] A. B. Jones and J. M. Smith, "Observation of rydberg blockade between two atoms," *Phys. Rev. Lett.*, vol. 13, 2013, p. 145.

[22] H. J. Metcalf and P. van der Straten, *Laser Cooling and Trapping*. Springer, 1999, ISBN: 0-387-98728-2.

[23] J. Dalibard and C. Cohen-Tannoudji, "Dressed-atom approach to atomic motion in laser light: the dipole force revisited," *J. Opt. Soc. Am. B*, vol. 2, 1985, p. 1707.

[24] M. J. Seaton, "Quantum defect theory," *Rep. Prog. Phys.*, vol. 46, 1983, p. 176.

[25] D. B. Branden, T. Juhasz, T. Mahlokozera, C. Vesa, R. O. Wilson, M. Zheng, A. Kortyna, and D. A. Tate, "Radiative lifetime measurements of rubidium rydberg states," *J. Phys. B:At. Mol. Opt. Phys.*, vol. 43, 2010, p. 015002.

[26] J. H. Hoogenraad and L. D. Noordam, "Rydberg atoms in far-infrared radiation fields. i. dipole matrix elements of h, li, and rb," *Phys. Rev. A*, vol. 57, 1998, p. 4533.

[27] P. Bohlouli-Zanjani, J. A. Petrus, and J. D. D. Martin, "Enhancement of rydberg atom interactions using ac stark shifts," *Phys. Rev. Lett.*, vol. 98, 2007, p. 203005.

[28] A. A. Khuskivadze, M. I. Chibisov, and I. I. Fabrikant, "Adiabatic energy levels and electric dipole moments of rydberg states of Rb_2 and Cs_2 dimers," *Phys. Rev. A*, vol. 66, 2002, p. 042709.

[29] V. A. Davydkin, B. A. Zon, N. L. Manakov, and L. P. Rapoport, "Quadratic stark effect on atoms," *Sov. Phys. JETP*, vol. 33, 1971, p. 70.

[30] L. Hostler, "Coulomb greens functions and the furry approximation," *Journal of Mathematical Physics*, vol. 5, 1963, p. 591.

[31] C. H. Greene, "Photoabsorption spectra of the heavy alkali-metal negative ions," *Phys. Rev. A*, vol. 42, 1990, p. 1405.

[32] C. Bahrim and U. Thumm, "Low-lying $^3P^o$ and $^3S^e$ states of Rb^-, Cs^-, and Fr^-," *Phys. Rev. A*, vol. 61, 2000, p. 022722.

[33] M. Marinescu, H. R. Sadeghpour, and A. Dalgarno, "Dispersion coefficients for alkali-metal dimers," *Phys. Rev. A*, vol. 49, 1994, p. 982.

[34] I. I. Fabrikant, "Theory of negative ion decay in an external electric field," *J. Phys. B:At. Mol. Opt. Phys.*, vol. 26, 1993, p. 2533.

[35] J. J. Sakurai, *Modern Quantum Mechanics*. Addison-Wesley Publishing Company, revised edition ed., 1994, p. 380, ISBN: 0-201-53929-2.

[36] M. I. Chibisov, A. A. Khuskivadze, and I. I. Fabrikant, "Energies and dipole moments of long-range molecular rydberg states," *J. Phys. B:At. Mol. Opt. Phys.*, vol. 35, 2002, p. L193.

[37] C. Bahrim1, I. I. Fabrikant, and U. Thumm, "Boundary conditions for the pauli equation: Application to photodetachment of Cs^-," *Phys. Rev. Lett.*, vol. 87, 2001, p. 123003.

[38] C. Bahrim1, U. Thumm, and I. I. Fabrikant, "$^3S^e$ and $^1S^e$ scattering lengths for e^-+Rb, Cs and Fr collisions," *J. Phys. B:At. Mol. Phys.*, vol. 34, 2001, p. L195.

[39] I. I. Fabrikant, "Interaction of rydberg atoms and thermal electrons with K, Rb and Cs atoms," *J. Phys. B:At. Mol. Phys.*, vol. 19, 1986, p. 1527.

[40] S. J. Buckman, "Atomic negative-ion resonances," *Rev. Mod. Phys.*, vol. 66, 1994, p. 539.

[41] R. K. Nesbet, *Variational Methods in Electron-Atom Scattering Theory*. Springer, 1980, p. 86, ISBN: 978-1-4684-8431-1.

[42] A. Gatan, Y. Miroshnychenko, T. Wilk, A. Chotia, M. Viteau, D. Comparat, P. Pillet, A. Browaeys, and P. Grangier, "Observation of collective excitation of two individual atoms in the rydberg blockade regime," *Nature Phys.*, vol. 5, 2009, p. 115.

[43] D. S. Weiss, E. Riis, Y. Shevy, P. J. Ungar, and S. Chu, “Optical molasses and multilevel atoms: experiment,” *J. Opt. Soc. Am. B*, vol. 6, 1989, p. 2072.

LIST OF PUBLICATIONS

1) R. Kaewuam, N. Chattrapiban, and W. Anukool, “Four Level Dynamic in Rubidium-85 Magneto-Optical Trap,” Proceedings, Siam Physics Congress, Krabi, Thailand, May 20 - May 22, 2015, pp. ATO5-ATO7.

APPENDIX A

Basis Wave Functions

In my calculation there are ten two-electron angular momentum basis in the LS representation expanded over $|\ell_1\ell_2 L M_L S M_S\rangle$ basis set with $M_J = 0$. The spin quantum numbers of two electrons are omiited because all electrons have the same spin 1/2. From Eq. (2.23) we obtain

$$
\begin{aligned}
& {}^{2S+1}L_{\mathrm{J}} = |\ell_1\ell_2 L M_L S M_S\rangle \\
1: \quad & {}^1S_0 = |000000\rangle \\
2: \quad & {}^3S_1 = |000010\rangle \\
3: \quad & {}^1P_1 = |011000\rangle \\
4: \quad & {}^3P_0 = \frac{1}{\sqrt{3}}|01111{-}1\rangle - \frac{1}{\sqrt{3}}|011010\rangle + \frac{1}{\sqrt{3}}|011{-}111\rangle \\
5: \quad & {}^3P_1 = \frac{1}{\sqrt{2}}|01111{-}1\rangle - \frac{1}{\sqrt{2}}|011{-}111\rangle \\
6: \quad & {}^3P_2 = \frac{1}{\sqrt{6}}|01111{-}1\rangle + \frac{2}{\sqrt{6}}|011010\rangle + \frac{1}{\sqrt{6}}|011{-}111\rangle \\
7: \quad & {}^1D_2 = |022000\rangle \\
8: \quad & {}^3D_1 = \sqrt{\frac{3}{10}}|02211{-}1\rangle - \sqrt{\frac{4}{10}}|022010\rangle + \sqrt{\frac{3}{10}}|022{-}111\rangle \\
9: \quad & {}^3D_2 = \frac{1}{\sqrt{2}}|02211{-}1\rangle - \frac{1}{\sqrt{2}}|022{-}111\rangle \\
10: \quad & {}^3D_3 = \frac{1}{\sqrt{5}}|02211{-}1\rangle + \sqrt{\frac{3}{5}}|022010\rangle + \frac{1}{\sqrt{5}}|022{-}111\rangle
\end{aligned}
\tag{A.1}
$$

Diagonal matrix elements are

$$
\begin{aligned}
D_{11} &= \frac{1}{R} & D_{66} &= \frac{1}{R} + \frac{1}{5}\frac{r^2}{R^3} \\
D_{22} &= \frac{1}{R} & D_{77} &= \frac{1}{R} + \frac{2}{7}\frac{r^2}{R^3} + \frac{2}{7}\frac{r^4}{R^5} \\
D_{33} &= \frac{1}{R} + \frac{2}{5}\frac{r^2}{R^3} & D_{88} &= \frac{1}{R} + \frac{1}{5}\frac{r^2}{R^3} \\
D_{44} &= \frac{1}{R} & D_{99} &= \frac{1}{R} + \frac{1}{7}\frac{r^2}{R^3} - \frac{4}{21}\frac{r^4}{R^5} \\
D_{55} &= \frac{1}{R} - \frac{1}{5}\frac{r^2}{R^3} & D_{1010} &= \frac{1}{R} + \frac{8}{35}\frac{r^2}{R^3} + \frac{2}{21}\frac{r^4}{R^5}
\end{aligned}
\tag{A.2}
$$

off-diagonal matrix elements are

$$
\begin{aligned}
D_{13} &= \frac{1}{\sqrt{3}}\left(\frac{r}{R^2} + \frac{\alpha_d}{r^2R^2}\right) & D_{46} &= -\frac{\sqrt{2}}{5}\frac{r^2}{R^3} \\
D_{17} &= \frac{1}{\sqrt{5}}\frac{r^2}{R^3} & D_{48} &= -\frac{\sqrt{2}}{3}\left(\frac{r}{R^2} + \frac{\alpha_d}{r^2R^2}\right) \\
D_{24} &= -\frac{1}{3}\left(\frac{r}{R^2} + \frac{\alpha_d}{r^2R^2}\right) & D_{410} &= -\frac{\sqrt{3}}{7}\frac{r^3}{R^4} \\
D_{26} &= \frac{\sqrt{2}}{3}\left(\frac{r}{R^2} + \frac{\alpha_d}{r^2R^2}\right) & D_{59} &= \frac{1}{\sqrt{5}}\left(\frac{r}{R^2} + \frac{\alpha_d}{r^2R^2}\right) - \frac{3}{7\sqrt{5}}\frac{r^3}{R^4} \\
D_{28} &= -\frac{\sqrt{2}}{5}\frac{r^2}{R^3} & D_{68} &= -\frac{7}{105}\left(\frac{r}{R^2} + \frac{\alpha_d}{r^2R^2}\right) - \frac{27}{105}\frac{r^3}{R^4} \\
D_{210} &= \frac{\sqrt{3}}{5}\frac{r^2}{R^3} & D_{610} &= \frac{\sqrt{6}}{5}\left(\frac{r}{R^2} + \frac{\alpha_d}{r^2R^2}\right) + \frac{2\sqrt{6}}{35}\frac{r^3}{R^4} \\
D_{37} &= \frac{2}{\sqrt{15}}\left(\frac{r}{R^2} + \frac{\alpha_d}{r^2R^2}\right) + \frac{3}{7}\sqrt{\frac{3}{5}}\frac{r^3}{R^4} & D_{810} &= -\sqrt{\frac{2}{3}}\left(\frac{10}{35}\frac{r^3}{R^4} + \frac{3}{35}\frac{r^2}{R^3}\right)
\end{aligned}
\tag{A.3}
$$

APPENDIX B

JJ-LS Transformation

The tranformation from jj representation into LS representation can be written as

$$|\ell_1\ell_2 LSJM_J\rangle = \sum_{j_1,j_2}^{J} C_{j_1,j_2}^{J,M_J} |\ell_1\ell_2 j_1 j_2 JM_J\rangle \tag{B.1}$$

where the coefficients C_{j_1,j_2}^{J,M_J} can be calculated from the following procedure. Starting from the expansion

$$|\ell_1\ell_2 LSJM_J\rangle = \sum_{M_L,M_S}^{M_J} C_{M_L M_S}^{J,M_J} |\ell_1\ell_2 LM_L SM_S\rangle\,, \tag{B.2}$$

where the basis vector $|\ell_1\ell_2 LM_L SM_S\rangle$ can be further expanded in uncoupld electron spinor as

$$|\ell_1\ell_2 LM_L SM_S\rangle = \left(\sum_{m_{\ell_1},m_{\ell_2}}^{M_L} C_{m_{\ell_1}m_{\ell_2}}^{L,M_L} |\ell_1 m_{\ell_1}\ell_2 m_{\ell_2}\rangle\right)\left(\sum_{m_{s_1},m_{s_2}}^{M_S} C_{m_{s_1}m_{s_2}}^{S,M_S} |m_{s_1}m_{s_2}\rangle\right) \tag{B.3}$$

Applying the same procedure with jj representation,

$$|\ell_1\ell_2 j_1 j_2 JM_J\rangle = \sum_{m_{j_1},m_{j_2}} C_{m_{j_1}m_{j_2}}^{J,M_J} |\ell_1\ell_2 j_1 m_{j_1} j_2 m_{j_2}\rangle \tag{B.4}$$

where

$$|\ell_1\ell_2 j_1 m_{j_1} j_2 m_{j_2}\rangle = \left(\sum_{m_{\ell_1},m_{s_1}} C_{m_{\ell_1}m_{s_1}}^{j_1,m_{j_1}} |\ell_1 m_{\ell_1} m_{s_1}\rangle\right)\left(\sum_{m_{\ell_2},m_{s_2}} C_{m_{\ell_2}m_{s_2}}^{j_2,m_{j_2}} |\ell_2 m_{\ell_2} m_{s_2}\rangle\right) \tag{B.5}$$

Due to the valence electron of the neutral atom is in s orbital, the quantum number ℓ_1 is alway zero. The jj representation naturally is used as appropriate basis for Dirac wave

function. Redefining the basis vector $|\ell_1\ell_2 j_1 j_2 J M_J\rangle$ by

$$|\kappa J M_J\rangle \equiv |\ell_1\ell_2 j_1 j_2 J M_J\rangle\,, \tag{B.6}$$

where κ is the relativistic quantum number used to define eigenstates of Dirac equation. In addition, the fundamental basis set $|\ell_1\ell_2 m_{\ell_1} m_{\ell_2} m_{s_1} m_{s_2}\rangle$ is defined as

$$\begin{aligned}
|\phi_1\rangle &= |0000\uparrow\downarrow\rangle & |\phi_6\rangle &= |010{-}1\uparrow\uparrow\rangle \\
|\phi_2\rangle &= |0000\downarrow\uparrow\rangle & |\phi_7\rangle &= |0201\downarrow\downarrow\rangle \\
|\phi_3\rangle &= |0101\downarrow\downarrow\rangle & |\phi_8\rangle &= |0200\uparrow\downarrow\rangle \\
|\phi_4\rangle &= |0100\uparrow\downarrow\rangle & |\phi_9\rangle &= |0200\downarrow\uparrow\rangle \\
|\phi_5\rangle &= |0100\downarrow\uparrow\rangle & |\phi_{10}\rangle &= |020{-}1\uparrow\uparrow\rangle
\end{aligned} \tag{B.7}$$

where the symbols $\uparrow$ and $\downarrow$ denote $m_s = 1/2$ and $m_s = -1/2$ respectively. Notice that all states in Eq. (B.7) corresponds with zero projection of total anular momoentum $M_J = 0$ and can be used to expand all states listed in Eq. (A.1).

$$\begin{pmatrix} |^1S_0\rangle \\ |^3S_1\rangle \\ |^1P_1\rangle \\ |^3P_0\rangle \\ |^3P_1\rangle \\ |^3P_2\rangle \\ |^1D_2\rangle \\ |^3D_1\rangle \\ |^3D_2\rangle \\ |^3D_3\rangle \end{pmatrix} = \begin{pmatrix} \frac{1}{\sqrt{2}} & \frac{-1}{\sqrt{2}} & 0 & 0 & 0 & 0 & 0 & 0 & 0 & 0 \\ \frac{1}{\sqrt{2}} & \frac{1}{\sqrt{2}} & 0 & 0 & 0 & 0 & 0 & 0 & 0 & 0 \\ 0 & 0 & 0 & \frac{1}{\sqrt{2}} & \frac{-1}{\sqrt{2}} & 0 & 0 & 0 & 0 & 0 \\ 0 & 0 & \frac{1}{\sqrt{3}} & \frac{-1}{\sqrt{6}} & \frac{-1}{\sqrt{6}} & \frac{1}{\sqrt{3}} & 0 & 0 & 0 & 0 \\ 0 & 0 & \frac{1}{\sqrt{2}} & 0 & 0 & \frac{-1}{\sqrt{2}} & 0 & 0 & 0 & 0 \\ 0 & 0 & \frac{1}{\sqrt{6}} & \frac{1}{\sqrt{3}} & \frac{1}{\sqrt{3}} & \frac{1}{\sqrt{6}} & 0 & 0 & 0 & 0 \\ 0 & 0 & 0 & 0 & 0 & 0 & 0 & \frac{1}{\sqrt{2}} & \frac{-1}{\sqrt{2}} & 0 \\ 0 & 0 & 0 & 0 & 0 & 0 & \sqrt{\frac{3}{10}} & \frac{-1}{\sqrt{5}} & \frac{-1}{\sqrt{5}} & \sqrt{\frac{3}{10}} \\ 0 & 0 & 0 & 0 & 0 & 0 & \frac{1}{\sqrt{2}} & 0 & 0 & \frac{-1}{\sqrt{2}} \\ 0 & 0 & 0 & 0 & 0 & 0 & \frac{1}{\sqrt{5}} & \sqrt{\frac{3}{10}} & \sqrt{\frac{3}{10}} & \frac{1}{\sqrt{5}} \end{pmatrix} \begin{pmatrix} |\phi_1\rangle \\ |\phi_2\rangle \\ |\phi_3\rangle \\ |\phi_4\rangle \\ |\phi_5\rangle \\ |\phi_6\rangle \\ |\phi_7\rangle \\ |\phi_8\rangle \\ |\phi_9\rangle \\ |\phi_{10}\rangle \end{pmatrix} \tag{B.8}$$

and for jj representation $|\kappa J\rangle$ we obtain

$$\begin{pmatrix} |-10\rangle \\ |-11\rangle \\ |10\rangle \\ |11\rangle \\ |-21\rangle \\ |-22\rangle \\ |21\rangle \\ |22\rangle \\ |-32\rangle \\ |-33\rangle \end{pmatrix} = \begin{pmatrix} \frac{1}{\sqrt{2}} & \frac{-1}{\sqrt{2}} & 0 & 0 & 0 & 0 & 0 & 0 & 0 & 0 \\ \frac{1}{\sqrt{2}} & \frac{1}{\sqrt{2}} & 0 & 0 & 0 & 0 & 0 & 0 & 0 & 0 \\ 0 & 0 & \frac{-1}{\sqrt{3}} & \frac{1}{\sqrt{6}} & \frac{1}{\sqrt{6}} & \frac{-1}{\sqrt{3}} & 0 & 0 & 0 & 0 \\ 0 & 0 & \frac{1}{\sqrt{3}} & \frac{1}{\sqrt{6}} & \frac{-1}{\sqrt{6}} & \frac{-1}{\sqrt{3}} & 0 & 0 & 0 & 0 \\ 0 & 0 & \frac{-1}{\sqrt{6}} & \frac{1}{\sqrt{3}} & \frac{-1}{\sqrt{3}} & \frac{1}{\sqrt{6}} & 0 & 0 & 0 & 0 \\ 0 & 0 & \frac{1}{\sqrt{6}} & \frac{1}{\sqrt{3}} & \frac{1}{\sqrt{3}} & \frac{1}{\sqrt{6}} & 0 & 0 & 0 & 0 \\ 0 & 0 & 0 & 0 & 0 & 0 & -\sqrt{\frac{3}{10}} & \frac{1}{\sqrt{5}} & \frac{1}{\sqrt{5}} & -\sqrt{\frac{3}{10}} \\ 0 & 0 & 0 & 0 & 0 & 0 & \sqrt{\frac{3}{10}} & \frac{1}{\sqrt{5}} & \frac{-1}{\sqrt{5}} & -\sqrt{\frac{3}{10}} \\ 0 & 0 & 0 & 0 & 0 & 0 & \frac{-1}{\sqrt{5}} & \sqrt{\frac{3}{10}} & -\sqrt{\frac{3}{10}} & \frac{1}{\sqrt{5}} \\ 0 & 0 & 0 & 0 & 0 & 0 & \frac{1}{\sqrt{5}} & \sqrt{\frac{3}{10}} & \sqrt{\frac{3}{10}} & \frac{1}{\sqrt{5}} \end{pmatrix} \begin{pmatrix} |\phi_1\rangle \\ |\phi_2\rangle \\ |\phi_3\rangle \\ |\phi_4\rangle \\ |\phi_5\rangle \\ |\phi_6\rangle \\ |\phi_7\rangle \\ |\phi_8\rangle \\ |\phi_9\rangle \\ |\phi_{10}\rangle \end{pmatrix} \tag{B.9}$$

Hence I can write LS representation in terms of jj representation

$$\begin{pmatrix} |^1S_0\rangle \\ |^3S_1\rangle \\ |^1P_1\rangle \\ |^3P_0\rangle \\ |^3P_1\rangle \\ |^3P_2\rangle \\ |^1D_2\rangle \\ |^3D_1\rangle \\ |^3D_2\rangle \\ |^3D_3\rangle \end{pmatrix} = \begin{pmatrix} 1 & 0 & 0 & 0 & 0 & 0 & 0 & 0 & 0 & 0 \\ 0 & 1 & 0 & 0 & 0 & 0 & 0 & 0 & 0 & 0 \\ 0 & 0 & 0 & \frac{1}{\sqrt{3}} & \sqrt{\frac{2}{3}} & 0 & 0 & 0 & 0 & 0 \\ 0 & 0 & -1 & 0 & 0 & 0 & 0 & 0 & 0 & 0 \\ 0 & 0 & 0 & \sqrt{\frac{2}{3}} & \frac{-1}{\sqrt{3}} & 0 & 0 & 0 & 0 & 0 \\ 0 & 0 & 0 & 0 & 0 & 1 & 0 & 0 & 0 & 0 \\ 0 & 0 & 0 & 0 & 0 & 0 & 0 & \sqrt{\frac{2}{5}} & \sqrt{\frac{3}{5}} & 0 \\ 0 & 0 & 0 & 0 & 0 & 0 & -1 & 0 & 0 & 0 \\ 0 & 0 & 0 & 0 & 0 & 0 & 0 & \sqrt{\frac{3}{5}} & -\sqrt{\frac{2}{5}} & 0 \\ 0 & 0 & 0 & 0 & 0 & 0 & 0 & 0 & 0 & 1 \end{pmatrix} \begin{pmatrix} |-10\rangle \\ |-11\rangle \\ |10\rangle \\ |11\rangle \\ |-21\rangle \\ |-22\rangle \\ |21\rangle \\ |22\rangle \\ |-32\rangle \\ |-33\rangle \end{pmatrix} \tag{B.10}$$

APPENDIX C

Quantum Dynamic of four-level system in magneto-optical trap

The physical system we study using the described formulation in the section 2.5 is a stationary four-level Rb-85 atom at center of MOT in the presence of cooling and repumping laser fields. The schematic of energy levels and detuning of fields with respect to transition is shown in Fig.(C.1). At the center of trap, the magnetic field is very small in which the Zeeman effect is negligible compared to the Rabi frequencies driven by the cooling and repumping laser fields. This approximation corresponds with an atom interacting with isotropic light polarization and it allows us to apply effective dipole transitions from $S_{1/2}, F$ to $P_{3/2}, F'$ without concerning sub-magnetic levels m_F. The field-free Hamiltonian of four-level atom is

$$\hat{H}_0 = \begin{pmatrix} \hbar\omega_1 & 0 & 0 & 0 \\ 0 & \hbar\omega_2 & 0 & 0 \\ 0 & 0 & \hbar\omega_3 & 0 \\ 0 & 0 & 0 & \hbar\omega_4 \end{pmatrix} \tag{C.1}$$

and the optical interaction with cooing beam and repumping beam are represented in interaction picture as

$$\hat{H}_I = \begin{pmatrix} 0 & \langle 1| V |2\rangle & 0 & 0 \\ 0 & \hbar\omega_2 & 0 & 0 \\ 0 & 0 & \hbar\omega_3 & 0 \\ 0 & 0 & 0 & \hbar\omega_4 \end{pmatrix} \tag{C.2}$$

By applying Eq.(2.69) to this system, the obtained optical Bloch equations are the system of first order coupled differential equations. Under a particular initial condition, the equations can be solved numerically.

In Figure C.2(a)-(b), we present the numerical solutions of optical Bloch equations

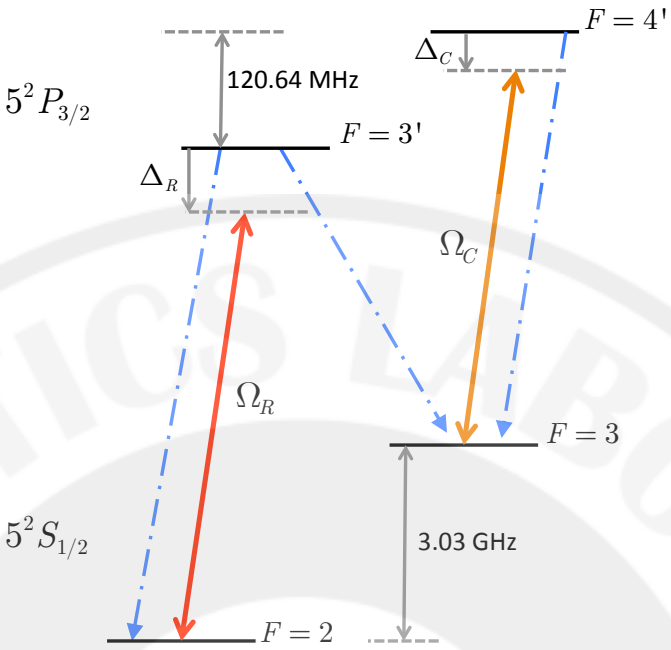

Figure C.1: The D2 line energy levels of rubidium-85. Hyperfine splitting of different F states of excited state $5^2P_{3/2}$ and ground state $5^2S_{1/2}$ are 120.6 MHz and 3.03 GHz respectively. The cooling light and repumping light have the detuning of Δ_C and Δ_R from resonance frequencies $F = 3 \rightarrow F = 4'$ and $F = 2 \rightarrow F = 3'$. Ω_C and Ω_R denote on-resonance Rabi frequencies of the two transitions. The spontaneous decay channels from $F = 3'$ and $F = 4'$ are shown by dash-doted blue line.

under two different initial conditions. The diagonal elements of density matrix are plotted as function of time and it denotes the evolution of probability of finding atoms occupying each hyperfine energy level. Figure C.2(a) shows the result where atom is initially in the lower ground state $F = 2$ and the populations reach the steady state at 2μs. This means at steady state of MOT the population of upper ground state $F = 3$ is dominate while there is around 20 percents atom occupying the excited state $F = 4'$. The result shown in Figure C.2(b) corresponds with the initial condition in which the population at the beginning equally distributes between the two ground states. Although these two initial conditions give the same steady state solutions, the main feature of the second condition is the beat-like fluctuation of populations in $F = 3$ and $F = 3'$. This beat oscillation happens due to the interference between two transitions $2 \rightarrow 3'$ and $3 \rightarrow 4'$ that have slightly different Rabi oscillation frequencies. Figure C.3 shows the time evolution of

coherence term relating to phase relation between $F = 3$ and $F = 3'$. According to the first condition, Figure C.3(a), the real part and imaginary part of the coherence term oscillate with equal amplitude and hence its trajectory reveals a helix curve. In the other hand, the coherence of the second initial condition, Figure C.3(b), has the behavior of perturbed-helical motion.

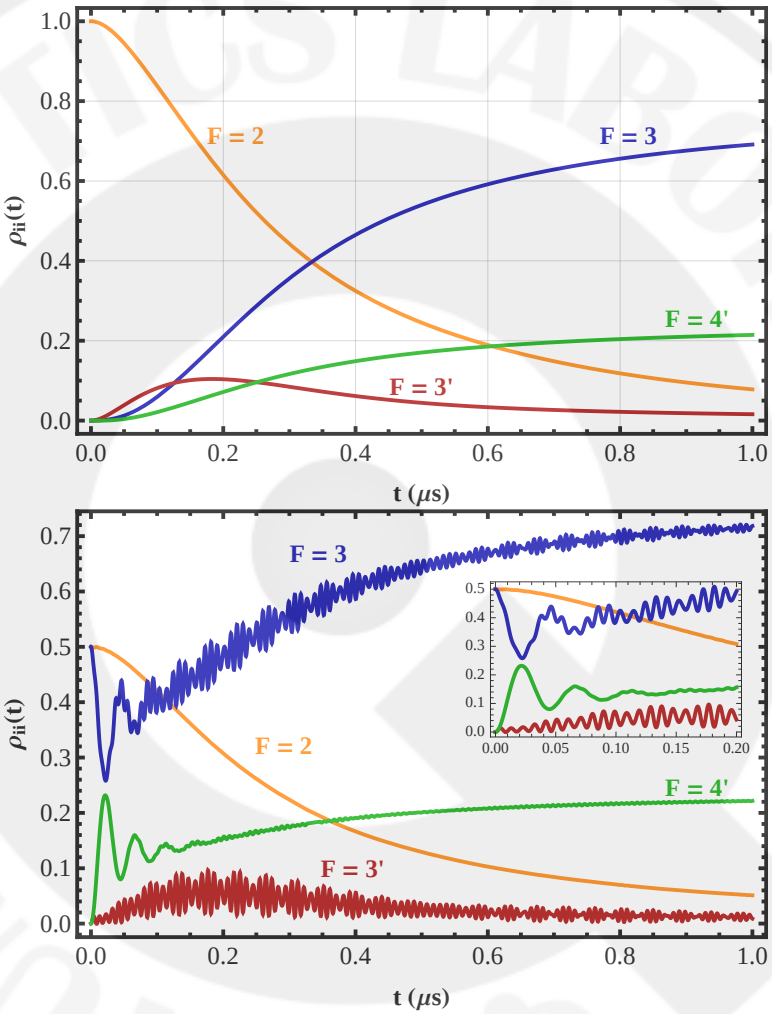

Figure C.2: Dynamic of populations under the presence of the cooling field and the repumping field. (a) atom is initially prepared in the ground state $F = 2$ and (b) the system starts from superposition of the two ground states, $F = 2$ and $F = 3$, with equal probability. The frequency of repumping field is on resonance while the detuning of cooling beam is of 2π(-14)MHz. The Rabi frequencies Ω_C and Ω_R are 114 MHz and 11.3 MHz respectively.

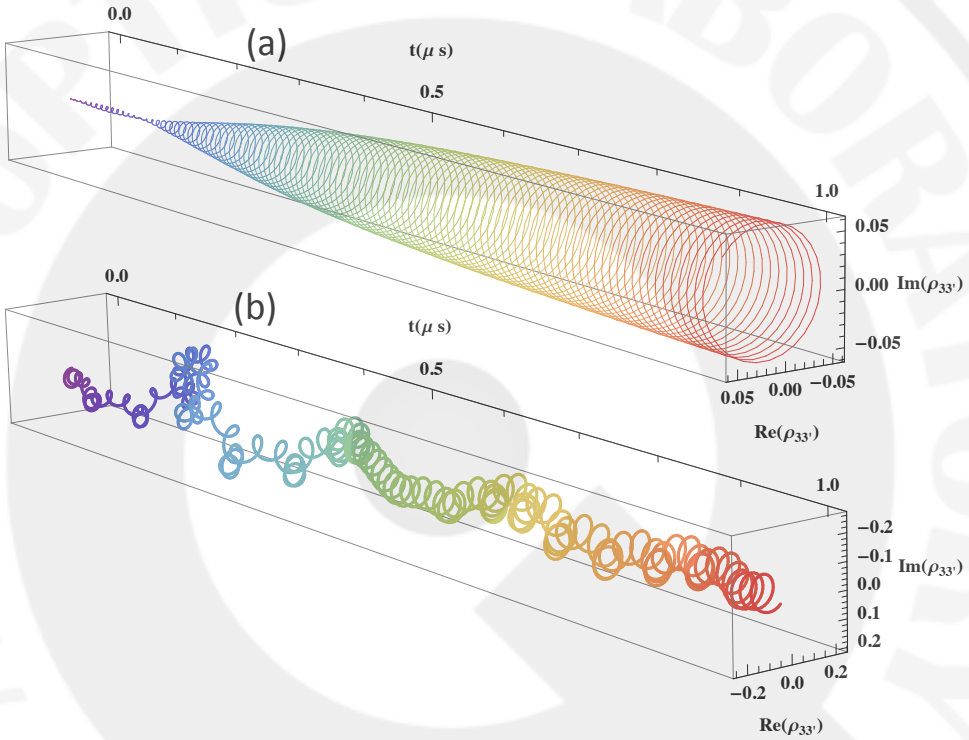

Figure C.3: The real and imaginary parts of coherence term $\rho_{33'}(t)$ as function of time: (a) atom is initially setup in lower ground state and (b) atom initially evolve from equal probability over two ground states.

CURRICULUM VITAE

Author's Name	Mr. Rattakorn Kaewuam	
Date/Year of Birth	14^{th} February 1990	
Place of Birth	Phichit Province, Thailand	
Education	2008-2011	Bachelor of Science in Physics Chiang Mai University, Chiang Mai, Thailand
	2005-2007	High School Diploma(Science-Mathematics) Phichipittayakom School, Phichi, Thailand
Scholarship	2010-present	Development and Promotion of Science and Technology Talents Project (DPST)
	2008-2009	Olympiad Physics
Experiences	2010-2014	Teaching Assistant: Electromagnetic theory Quantum Mechanics Classical Mechanics